ACS APPLIED MATERIALS & INTERFACES

www.acsami.org

Research Article

Oxidant-Free Atomic Layer Deposition of SnO_2 Using Complementary Metal Precursors

Alejandra Ruiz-Clavijo,* Amin Bahrami, Jonathan E. Rodriguez Hueso, Jaakko Julin, Noel Israel, Angelika Wrzesińska-Lashkova, Daniel Wolf, Nithin Thonakkara James, Sebastian Lehmann, Jonathan Guerrero-Sánchez, R. Ponce-Perez, Alexey A. A. Popov, Manuel Dominguez, Yana Vaynzof, Kaline P. Furlan, Eduardo Blanco, and Kornelius Nielsch*

Cite This: https://doi.org/10.1021/acsami.6c07074

Read Online

ACCESS | Metrics & More | Article Recommendations | Supporting Information

ABSTRACT: We report a novel atomic layer deposition (ALD) process for SnO_2 that does not require water or other strong oxidizing agents, such as H_2O, O_2 plasma, O_3, or H_2O_2. The development of alternative oxidant-free ALD processes is highly attractive because it enables a gentler and more controllable chemical environment, which is crucial for next-generation nanoscale devices and complex material stacks. In this approach, Sn-based complementary metal precursors are employed: $Sn(OtBu)_4$ serves as both the tin and oxygen precursor, while $SnCl_4$ acts as an additional tin source. For this precursor combination, an optimal ALD temperature window of 70–90 °C was established, within which amorphous SnO_2 films are deposited. Post-deposition annealing is subsequently required to develop the desired crystallinity and to adjust the oxygen-vacancy concentration and impurity levels, which ultimately determine the electrical and optical properties of the resulting SnO_2 films and their potential for various applications. To gain mechanistic insight into this oxidant-free SnO_2 growth process, we employ density functional theory (DFT) calculations to investigate the surface reactions during sequential exposure of $Sn(OtBu)_4$ and $SnCl_4$ on a SiO_2 substrate. The results reveal key atomic-level processes, including ligand-exchange pathways, oxygen transfer, and surface regeneration, which govern film growth. This combined experimental and theoretical approach provides fundamental understanding of the SnO_2 ALD mechanism and offers guidance for post-deposition optimization of the material.

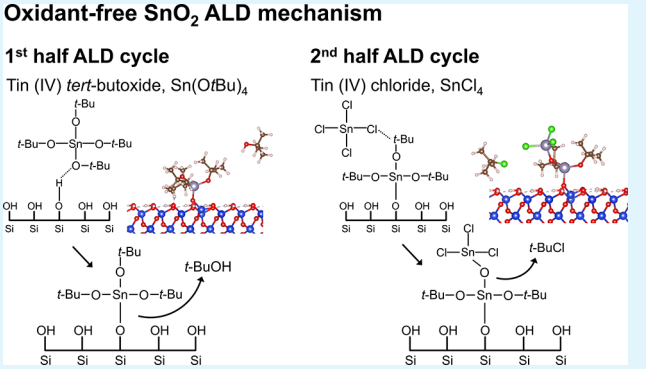

KEYWORDS: *tin(IV) oxide, atomic layer de position (ALD), oxidant-free ALD, water-free ALD, low-temperature deposition, thin films, sensitive substrates, hydrophobic substrates*

1. INTRODUCTION

Tin(IV) oxide (SnO_2) is a technologically important wide-band-gap transparent oxide widely used in optoelectronic and photonic devices owing to its high transparency in the visible and near-infrared regions, moderate to high refractive index (1.9–2.1), and excellent chemical and thermal stability.[1−4] When doped, SnO_2 also exhibits appreciable electrical conductivity, enabling its implementation in solar cells, flat-panel displays, transparent electrodes, and gas sensors.[5−10] IntegratingSnO_2 into increasingly complex device architectures, however, requires deposition techniques capable of delivering conformal, uniform films, with precise thickness control under substrate-compatible conditions.

SnO_2 thin films can be deposited using various physical and chemical techniques.[11] Among them, atomic layer deposition (ALD) stands out as a particularly attractive approach, as it can overcome many of the challenges associated with implementing this material in practical device architectures. Owing to its self-limiting surface reactions, ALD enables precise thickness control, excellent uniformity, and conformal coating of high-aspect-ratio and complex geometries. These characteristics are essential for interface engineering in photovoltaic devices,[6,10,12] and functionalizing nanostructured sensing platforms,[13] where maximizing surface-area-to-volume ratio directly impacts performance.

Received: April 8, 2026
Revised: August 20, 2026
Accepted: August 24, 2026

As a result, considerable research efforts have been devoted to process development for the ALD growth of SnO_2 thin films. However, relatively few studies address the need for less aggressive reaction conditions compatible with sensitive substrates, such as carbon-based materials, polymeric opal structures or in multilayers stacks, which are increasingly relevant for advanced photonic and sensing applications. Conventional ALD processes relying on strong oxidants can damage or unintentionally modify underlying layers by oxidizing metals, 2D materials, or organic components. In semiconductor stacks such as Si, Ge, or III–V materials, this often leads to interface degradation. In contrast, oxidant-free processes help preserve these delicate surfaces, enabling improved integration with organic electronics, 2D materials such as graphene and MoS_2, as well as metal contacts without inducing parasitic oxidation.

The ability to deposit high-quality SnO_2 conformally on delicate templates, such as self-assembled polymeric opals, and within multilayer architectures highlights the broader potential of oxidant-free deposition processes for fabricating compositionally and structurally versatile materials, which could enable a wide range of applications, including three-dimensional photonic crystals with tunable optical band gaps, enhanced light-matter interactions, and improved performance in optical sensors[14,15] light-harvesting systems,[16,17] and photocatalysis.[18]

Preceding work on this topic was carried out by Marichy et al., who demonstrated the growth of SnO_2 using $Sn(OtBu)_4$ and acetic acid (CH_3COOH).[1,13] In other studies, more reactive oxidants such as NO or N_2O_4 have been explored to reduce the deposition temperature; however, these approaches do not address the issue of substrate oxidation damage.[19,20]

The work presented here adopts a different precursor chemistry approach. Our precursor combination was inspired by a previously developed ALD process for SbO_x established within our group, in which complementary Sb-based metal precursors were successfully employed.[21] Accordingly, two complementary Sn-based metal precursors were deliberately selected to favor a ligand-exchange reaction over the conventional oxidation of the Sn precursor by an oxidizing co-reactant.[22−28] Although both the present work and that of Marichy et al.[1,13] are governed by ligand-exchange reactions, the use of complementary Sn-based precursors in the present process enables an optimal deposition temperature below 100 °C (70–90 °C), whereas their process operates at 150–175 °C. Moreover, our method achieves a growth per cycle (GPC) of 0.12 nm cycle^{-1} at 80 °C, significantly exceeding the 0.07 nm cycle^{-1} reported in their study at 150 °C. At a comparable deposition temperature of 75 °C, their process exhibits a GPC of only 0.03 nm cycle^{-1}. The newly developed water-/oxidant-free SnO_2-ALD recipe, presented here, is tested on delicate substrates to evaluate its compatibility with temperature-sensitive, hydrophobic, and readily oxidized materials, such as polymeric opals, as well as within multilayer semiconductor/oxide stacks.

Another remarkable aspect of this work is the effort to unify experimental investigations with density functional theory (DFT) calculations, providing insight into the atomistic mechanisms governing oxidant-free SnO_2 ALD, which remain largely unexplored. To address this gap, we combine experiments with DFT calculations to resolve the elementary surface reactions that occur during alternating $Sn(OtBu)_4$ and $SnCl_4$ exposure on a SiO_2 substrate. These calculations reveal adsorption configurations, ligand-exchange pathways, and surface regeneration steps. Our results demonstrate that oxygen transfer from $Sn(OtBu)_4$ enables oxide formation without external oxidants and identify the energetically preferred ligand-elimination sequence. We further identify the rate-limiting steps and competing pathways responsible for residual chlorine incorporation and oxygen vacancy formation—key factors governing the films' electrical and optical properties. These studies establish a mechanistic framework linking precursor chemistry to defect formation and self-limiting growth in low-temperature SnO_2 ALD process.

2. RESULTS AND DISCUSSION

2.1. SnO_2 ALD Parameters

We report the atomic layer deposition of SnO_2 thin films using $SnCl_4$ as the tin precursor and $Sn(OtBu)_4$ as both tin and oxygen source. The specific ligand exchange sequence is further supported by density functional theory calculations that investigate the reaction pathways in this oxidant-free environment (see the following section on Computational studies of the ALD Growth Mechanism).

This approach avoids the use of external oxidizing agents, which is advantageous for substrates sensitive to strong oxidants (e.g., O_2, O_3, H_2O_2) or water repellent (hydrophobic surfaces), while also enabling deposition at reduced temperatures. Figure 1a shows the growth per cycle (GPC) as a function of deposition temperature. A well-defined ALD window is observed between 70 and 90 °C, within which the GPC remains constant at ∼0.10 nm cycle^{-1}. At temperatures above 90 °C, thermal decomposition of $Sn(OtBu)_4$ becomes significant,[1,2] leading to a continuous increase in GPC up to the maximum studied temperature of 120 °C. The observed ALD window lies below the temperature range commonly reported for SnO_2 ALD, for which deposition temperatures above 150 °C are frequently employed.[1,2,6,22−28] Although SnO_2 deposition below 100 °C has been previously reported,[29−32] most of these early reports do not provide evidence for self-limiting ALD growth at such low temperatures. In addition, the increase in GPC with decreasing deposition temperature observed in some of these studies is inconsistent with a well-defined ALD growth regime, being an indicator of potential precursor condensation at lower temperatures.[30] Moreover, the stable ALD window reported in these studies generally begins at 100 °C or higher.[1,24,29−31]

To investigate the self-limiting nature of the ALD process, depositions were carried out at 80 °C, and the GPC was evaluated as a function of precursor pulse duration. As shown in Figure 1b,c, saturation behavior is observed with a 0.15 s pulse of $Sn(OtBu)_4$ and a 0.01 s pulse of $SnCl_4$, beyond which the GPC plateaus. This confirms the self-limiting reaction mechanism characteristic of ALD. Based on these results, the precursor pulse durations were set to 0.15 s for $Sn(OtBu)_4$ and 0.01 s for $SnCl_4$, resulting in a stable GPC of 0.12 nm cycle^{-1}. The lower GPC of ∼0.10 nm cycle^{-1} observed in Figure 1a reflects the use of non-optimized precursor pulse durations during the initial temperature-dependent study. Following process optimization, a linear relationship between film thickness and the number of ALD cycles was observed (Figure 1d), further confirming the self-limiting and layer-by-layer nature of the ALD process. The standard deviation of the thickness measurements was found to be in the range of 1–2.5 nm (see Figure S1a,b).

https://doi.org/10.1021/acsami.6c07074
ACS Appl. Mater. Interfaces XXXX, XXX, XXX−XXX

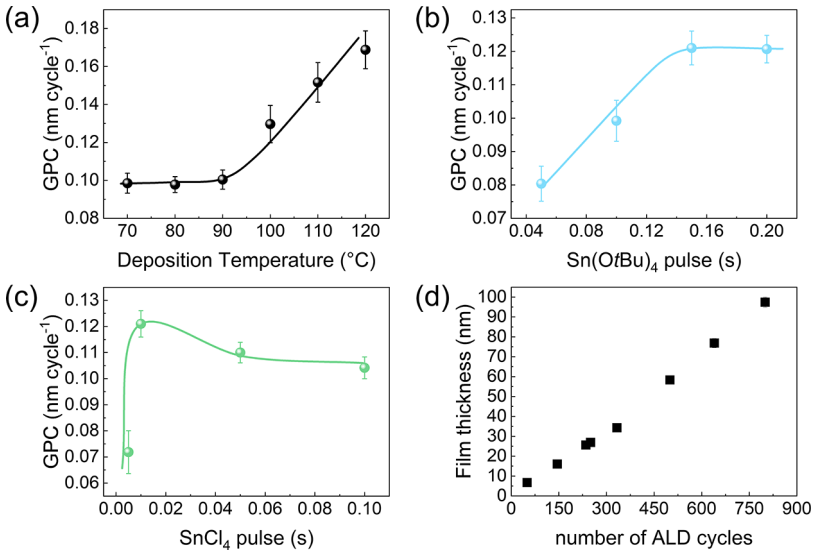

Figure 1. ALD parameters of SnO_2 growth process: (a) GPC temperature dependency. (b) GPC as a function of $Sn(OtBu)_4$ pulse length, while the $SnCl_4$ pulse and purge are set to 0.01 and 10 s, respectively. (c) GPC as a function of $SnCl_4$ pulse length, $Sn(OtBu)_4$ pulse and purge set at 0.15 and 10 s, respectively. (d) Film thickness with the number of applied ALD cycles. Figures (b–d) were obtained fixing the deposition temperature at 80 °C.

2.2. Morphological, Structural, and Compositional Characterization of SnO_2 Films

Scanning electron microscopy (SEM) images of as-grown films (Figure 2a) reveal a smooth surface without discernible features, characteristic of an amorphous morphology. This observation is corroborated by in situ X-ray diffraction (XRD) measurements acquired during heating from 30 to 500 °C in air (Figure S2a, Supporting Information). No diffraction peaks are observed up to 350 °C, confirming that the as-grown SnO_2 ALD films are amorphous. Crystallization onset occurs at temperatures ≥350 °C; therefore, an annealing temperature of 450 °C was selected for subsequent experiments. Similar to the present work, SnO_2 films deposited at low temperatures (≤200 °C) are typically amorphous.[22,24,29–31]

In contrast, films annealed at 450 °C under Ar (Figure 2b), O_2 (Figure 2c), and air (Figure 2d) exhibit a granular texture. The grain size strongly depends on the annealing atmosphere: annealing in Ar yields larger grains and agglomerates above 10 nm, whereas annealing in O_2 or air yields significantly smaller grains, with average sizes below 10 nm.

Figure 2e presents the ex situ XRD patterns of as-grown and Ar-, O_2- and air-annealed films at 450 °C (bottom to top). All samples exhibit identical diffraction patterns, corresponding to the tetragonal SnO_2 phase (space group $P42/mnm$). The main reflections are observed at $2\theta = 26.84°$ and 34.30°, which are assigned to the (110) and (101) planes, respectively, along with a weaker peak at 37.92° corresponding to the (200) plane. The films are highly polycrystalline, with no evidence of preferred orientation. Crystallite size (D) analysis using the Scherrer method indicates average nanocrystallite sizes of 6.9, 3.6, and 3.0 nm for films annealed in Ar, air, and O_2, respectively, which is consistent with the grain sizes observed by SEM. Although relatively few studies explicitly report crystallite sizes for SnO_2 films prepared under comparable conditions, Marichy et al. reported grain sizes below 10 nm.[1–13] Likewise, Chen et al. observed an increase in grain size from 1.23 to 5.30 nm with increasing annealing temperature.[6] These values are in good agreement with those obtained in the present study.

SnO_2 films analyzed by AFM (Figure S3a–d) show that the as-deposited layers at 80 °C present low roughness values (S_q ≈ 0.35 nm). Upon annealing, the surface roughness increases and follows the same trend as the crystallite size, indicating that the observed grain growth drives surface roughening (see Table 3). Ar- and air-annealed films exhibit the highest roughness (S_q ≈ 1.82 and 1.76 nm, respectively), while O_2-annealed films remain comparatively smooth (S_q ≈ 0.49 nm), consistent with their smaller crystallite size. Such low roughness values are typically observed in amorphous SnO_2 films and generally increase with increasing crystallinity. However, the surface morphology is also influenced by other factors, including deposition temperature, film thickness, post-deposition treatment, and the choice of metal precursor (see Table S2).

For example, studies employing $SnCl_4$ as a precursor (as in this work) typically report higher roughness values (S_q = 3–10 nm), scaling with the film thickness (35–100 nm).[27] It should be noted that these studies generally employ deposition temperatures above 200 °C, whereas the present process was carried out at significantly lower temperatures. As a result, SnO_2 films obtained in this work exhibit substantially lower surface roughness, even after annealing.

The surface composition and chemical oxidation states of the elements in SnO_2 films, as-grown and annealed, were analyzed using X-ray photoemission spectroscopy (XPS). To probe deeper into the film bulk, samples were etched with an Ar beam for 300 s immediately before measurement. High-resolution XPS spectra of Sn 3d, O 1s, and Cl 2p are shown in Figure 3a–c. For comparison, samples were initially measured without any etching, and the corresponding XPS spectra are shown in Figure S4a–c of the Supporting information.

The Sn 3d spectra (Figure 3a) of the annealed SnO_2 films—regardless of the annealing atmosphere—exhibit two distinct peaks at approximately 486.9 and 495.3 eV, corresponding to the Sn $3d_{5/2}$ and Sn $3d_{3/2}$ spin-orbit components, respectively. These binding energies (BEs) are indicative of Sn^{4+} oxidation state, consistent with the formation of SnO_2,[33,34] and align with XRD results. In addition, the valence band spectra of the films

https://doi.org/10.1021/acsami.6c07074
ACS Appl. Mater. Interfaces XXXX, XXX, XXX–XXX

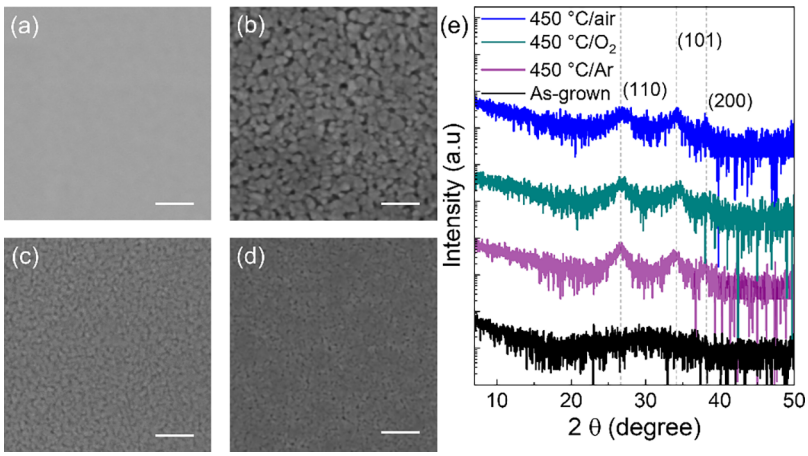

Figure 2. (a–d) Top-view SEM images of SnO_2 thin films: (a) as-deposited and after annealing at 450 °C in (b) Ar, (c) O_2, and (d) air. The scale bar is 100 nm. (e) ex situ XRD diffractograms of SnO_2 films as-grown (black), and annealed films at 450 °C under Ar (purple), O_2 atmosphere (green), and in ambient conditions (blue).

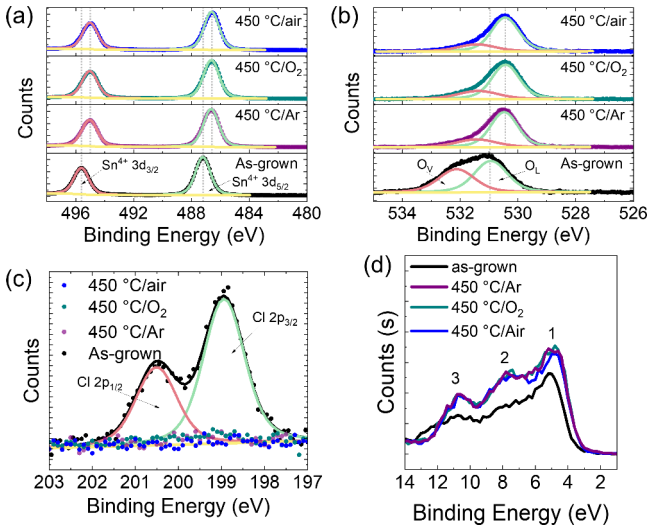

Figure 3. XPS spectra of (a) Sn 3d, (b) O 1s, and (c) Cl 2p orbitals of SnO_2 films as as-grown (black) and after annealing at 450 °C in Ar (purple), O_2 (green) and in ambient conditions (blue). (d) Valence band spectra of SnO_2 films.

(Figure 3d) further confirm the successful growth of SnO_2, since the peaks located at approximately 4.7, 7.4, and 10.5 eV (1 to 3) are characteristic of SnO_2. No features associated with SnO are observed, which would typically appear at around 3.0, 6.5, and 9.7 eV.[35]

However, the peaks in the as-grown film are shifted towards higher binding energies (~487.3 and 495.7 eV). This shift reflects the distinct chemical environment of this sample, which exhibits the highest impurity content (H, C, and Cl; see Tables 1 and 2). These electron-withdrawing species reduce the local electron density around Sn (and O) atoms, resulting in higher core-level binding energies. The amorphous nature of the as-grown film may also play a role, as the lack of long-range order and the associated distribution of local coordination environments can lead to additional binding energy broadening and shifts.[36]

The presence of these impurities indicates incomplete ALD reactions at low deposition temperature, driven by incomplete surface reactions and steric hindrance associated with the bulky $Sn(OtBu)_4$ precursor (see Computational Section), leading to residual ligand species trapped in the film. Carbon originates from the $Sn(OtBu)_4$ precursor (Figure S5), whereas chlorine (Figure 3c), originating from the $SnCl_4$ precursor, is incorporated into the film primarily at oxygen vacancy sites.[37−39] Following annealing at 450 °C under any of the tested atmospheres, the carbon signal is drastically reduced (Figure S5), while chlorine becomes undetectable, indicating effective impurity removal from the films. Only a small Cl atomic percentage (~0.5%) is still detected in the O_2-annealed samples by XPS (Table 1); however, ERDA measurements indicate a significantly lower value (~0.12 at%, Table 2). As the Cl XPS signal for this sample is not well defined (see Figures S6a,b in the Supporting Information), this likely leads to an overestimation of the chlorine content in the XPS analysis.

The O 1s spectra (Figure 3b) show a broad peak that can be deconvoluted into two components centered at 530.5 and 531.5 eV for the annealed films. As previously noted, for the as-grown film, the O 1s signal is also shifted to higher BEs, appearing at 531 and 532.2 eV. This shift is attributed to the same factors discussed above. In addition, impurity-related passivation of oxygen vacancies is reported to further contribute to this shift.[40]

The lower binding energy peak (O_L) corresponds to lattice oxygen (Sn–O bonds), while the higher energy peak (O_V) is associated with oxygen vacancies.[41,42] These vacancies can be occupied by chemisorbed oxygen, hydroxyl groups, or other impurities such as chlorine. The O_L/O_V ratio varies after the annealing step, as detailed in Table 1. The as-grown film exhibits the highest percentage of oxygen vacancies, ranging from 45–47%, while after annealing, the percentage of O_V reduces by nearly half. This suggests that during annealing, impurities such as C, H, and Cl are removed concomitantly with crystallization (as indicated by ERDA analysis of light elements, Table 2), thereby promoting the formation of Sn–O bonds. In fact, the O/Sn ratio increases from 1.6 to 1.8–1.9, approaching the stoichiometric value of 2. Note that, for this calculation, only the lattice oxygen (O_L) contribution was considered.[2]

Additionally, slight variations in the number of oxygen vacancies were observed depending on the annealing atmosphere

https://doi.org/10.1021/acsami.6c07074
ACS Appl. Mater. Interfaces XXXX, XXX, XXX−XXX

Table 1. Elemental Composition of the SnO_2 Films, as Determined by XPS

sample	etching time (s)	Sn [at%]	O_{total} [at%]	O_L [at%]	O_V [at%]	Cl [at%]	O_V/O_{total} %	O_L/Sn ratio [at/at]
as-grown		15.25	46.43	24.71	21.72	3.74	47	1.62
	300 s	16.07	47.52	26.25	21.27	3.65	45	1.63
450°C/Ar		25.69	62.64	44.34	18.30		29	1.72
	300 s	26.57	63.46	47.77	15.69		25	1.80
450°C/O_2		26.68	64.28	49.08	15.20	0.52	24	1.84
	300 s	26.76	64.32	47.70	16.62	0.49	26	1.78
450°C/air		26.72	64.86	51.02	13.84		21	1.91
	300 s	27.06	65.07	50.84	14.23		22	1.88

Table 2. Elemental Composition of the SnO_2 Films Based on ToF-ERDA Measurements

sample	H [at%]	C [at%]	N [at%]	O [at%]	Cl [at%]	Sn [at%]	O/Sn ratio [at/at]
as-grown	18.9 ± 0.9	1.3 ± 0.3	0.6 ± 0.2	44.3 ± 1.1	12.2 ± 0.7	22.6 ± 0.6	1.60 ± 0.02
450°C/Ar	2.4 ± 0.4	1.6 ± 0.4	<0.3	63.9 ± 0.5	< 0.1	32.1 ± 0.4	1.98 ± 0.02
450°C/O_2	6.1 ± 0.6	2.7 ± 0.4	0.5 ± 0.2	60.0 ± 0.6	0.12 ± 0.04	30.6 ± 0.4	1.98 ± 0.02
450°C/air	3.6 ± 0.5	1.0 ± 0.3	<0.3	62.9 ± 0.5	< 0.1	32.4 ± 0.4	1.99 ± 0.02

(Ar, O_2, and air). Ar-annealed films show 25–29% O_V, while those annealed in O_2 and air exhibit slightly reduced percentages of O_V, ranging from 24–26% and 21–22%, respectively. This reduction can be attributed to the incorporation of oxygen from the surrounding environment during annealing.

The ToF-ERDA depth profiles of the as-deposited and annealed SnO_2 films (Figure S7a–d) show that the films are primarily composed of tin and oxygen throughout their thickness, with a rather homogeneous composition profile. However, varying levels of chlorine, carbon, and hydrogen contamination are also detected, depending on the specific film and annealing conditions. For example, in the as-grown SnO_2 film shown in Figure S7a, the Cl and H profiles are clearly distinguishable, each exceeding 10 at%. The average composition (in at%) of each film is summarized in Table 2. These values were calculated within the depth range defined by the vertical lines in the profiles, thereby excluding both the surface region and the film-substrate interface.

For the as-grown SnO_2 film, the measured O/Sn ratio is 1.60, which is significantly lower than the stoichiometric value of 2.00. During ERDA analysis, this sample exhibits pronounced irradiation-induced damage accompanied by detectable oxygen loss, which can be attributed to the presence of weakly bonded oxygen species and high impurity levels. In particular, hydrogen and chlorine are detected at high concentrations of 18.9 and 12.2 at%, respectively, whereas carbon is relatively low (1.3 at%). These results indicate incomplete ALD reactions, leading to defect-rich, impurity-containing films. This interpretation is consistent with the XPS analysis, which shows a high oxygen-vacancy-related component (O_V) that accounts for approximately 45–47% of the total O 1s signal for this sample. This behavior is commonly attributed to incomplete surface reactions at low deposition temperatures (≤100 °C), which result in residual organic ligands being incorporated into the films. Consequently, relatively high carbon and nitrogen impurity concentrations (>10 at%) are often reported.[24,29−31] In contrast, chlorine and hydrogen are the predominant impurities in the present films, reflecting the different precursor chemistry employed, with carbon content remaining low (≈1 at%) in the as-grown films. Impurity levels reported by other low temperature SnO_2 processes are also summarized in Table S2.

Annealing significantly improves the Sn–O bonding efficiency, yielding O/Sn ratios of 1.98 ± 0.02 for all annealed films, approaching the stoichiometric value of 2.00. No measurable irradiation-induced damage or oxygen loss is observed, indicating stronger Sn–O bonding and enhanced film stability, resulting from the effective removal of residual impurities, in particular hydrogen and chlorine. Carbon levels remain low (1.0–1.6 at%), except for the SnO_2 film annealed in O_2, which shows a slightly higher carbon content (2.3 at%).

Ar-annealed films exhibit markedly reduced hydrogen (2.4 at%) and the chlorine below the detection limit (<0.1 at%), whereas ambient-air annealing yields slightly higher hydrogen (3.6 at%) due to ambient humidity, with chlorine still <0.1 at%. The O_2-annealed film shows higher residual hydrogen (6.1 at%) and carbon (2.7 at%), suggesting either increased contamination during deposition or during O_2 annealing.

Overall, ERDA and XPS analyses show that annealing effectively removes impurities and improves Sn–O bonding, even when the chemical reactions occurring during the ALD process carried out at 70–90 °C are not fully completed. Complementary SEM and XRD results further indicate that annealing promotes enhanced crystallinity, as discussed before. AFM analysis shows that the surface roughness increases following the trend as-grown < O_2-annealed < air-annealed < Ar-annealed, consistent with the observed increase in grain size.

2.3. Computational Study of the ALD Growth Mechanism of SnO_2

To simulate the reported growth of SnO_2 thin films using SiO_2 as the substrate, $SnCl_4$ as the tin precursor, and $Sn(OtBu)_4$ as both oxygen and tin source, the first step was to construct and optimize the structural models for each component. The SiO_2 surface was derived from the optimized bulk structure. As illustrated in Figure S9 of the Supporting Information, the unit cell was expanded to a 4 × 4 supercell to minimize lateral interactions between periodically repeated adsorbates and to enable the modeling of isolated adsorption events. To obtain a chemically stable and experimentally representative interface, the undercoordinated surface O atoms were terminated with hydroxyl (–OH) groups, and the structure was fully relaxed

https://doi.org/10.1021/acsami.6c07074
ACS Appl. Mater. Interfaces XXXX, XXX, XXX–XXX

before adsorption calculations. A slab was cleaved from the supercell along the z direction to generate a surface termination, with a 15 Å vacuum region perpendicular to the surface to eliminate periodic interactions. This hydroxylated slab provides a realistic representation of oxide surfaces under typical ALD conditions, and forms the basis for studying precursor adsorption and surface reactions during SnO_2 film growth.

To describe the molecular structures of the Sn-based precursors employed in this study, the geometries of tin(IV) chloride ($SnCl_4$) and tin(IV) *tert*-butoxide [$Sn(OtBu)_4$] were constructed and fully optimized (Figure 4).

$SnCl_4$ exhibits a tetrahedral coordination geometry, with the Sn center symmetrically bonded to four chlorine atoms. This highly symmetric configuration results in a compact molecule with strong Sn–Cl bonds and no intrinsic oxygen ligands. Consequently, surface reactions involving $SnCl_4$ typically proceed through ligand-exchange mechanisms with surface oxygen species, particularly hydroxyl (–OH) groups. In contrast, $Sn(OtBu)_4$ features a tetracoordinated Sn center bonded to four alkoxide ligands via Sn–O bonds. The presence of preformed Sn–O linkages in this precursor serves as an internal oxygen source in the ALD process investigated here, facilitating direct oxygen transfer to the growing film during surface reactions.

The distinct chemical nature of these two precursors (halide and alkoxide) leads to fundamentally different adsorption behaviors and reaction pathways during SnO_2 growth. A detailed understanding of their molecular structures is therefore essential to rationalize the energetics, reaction mechanisms, and growth characteristics observed throughout the ALD cycle.

To probe the adsorption mechanisms, electrostatic potential maps (EPMs) were employed to analyze the charge distribution on both the surface and the precursor molecules (Figure S10). Reactive sites were identified by locating regions of complementary electrostatic potential: red (electron-rich, negative potential), blue (electron-deficient, positive potential), and green (near-neutral). Interactions are favored between regions of opposite electrostatic character. Based on the identification of these complementary sites, the proposed ligand-exchange pathways were constructed.

The first half-cycle of the ALD process was investigated by analyzing the reaction pathway of the $Sn(OtBu)_4$ precursor on the hydroxylated SiO_2 surface. Figure 5a presents the optimized geometries corresponding to the initial state (IS), transition state (TS), and final state (FS) along the ligand-exchange pathways. In the initial state (IS), the precursor interaction is dominated by weak physisorption with a reactive ligand oriented toward a surface –OH. The transition state (TS) corresponds to the stage where the surface hydroxyl interacts with the precursor, initiating ligand dissociation and facilitating Sn–O bond formation via proton transfer, with the TS configuration at 0.15 eV. In the final state (FS), the precursor becomes chemically anchored to the surface through the formation of a stable Sn–O bond, while the eliminated ligand reacts with a surface hydrogen atom to form *tert*-butanol (2-methyl-2-propanol, $COH(CH_3)_3$) as a byproduct. The system relaxes to 0.11 eV at the FS, where the adsorbed fragment attains a stable configuration. The energetics suggest that the hydroxylated surface efficiently promotes precursor activation and Sn–O bond formation under oxidant-free conditions.

In the second half-cycle, $SnCl_4$ reacts with the surface species generated in the first half-cycle (Figure 5b). In the initial state

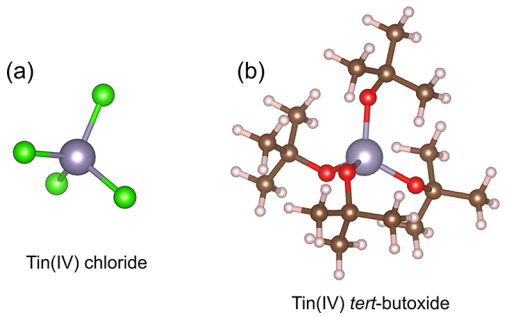

Figure 4. Optimized molecular structures of the Sn precursors used in this study: (a) tin(IV) chloride ($SnCl_4$) and (b) tin(IV) *tert*-butoxide [$Sn(OtBu)_4$].

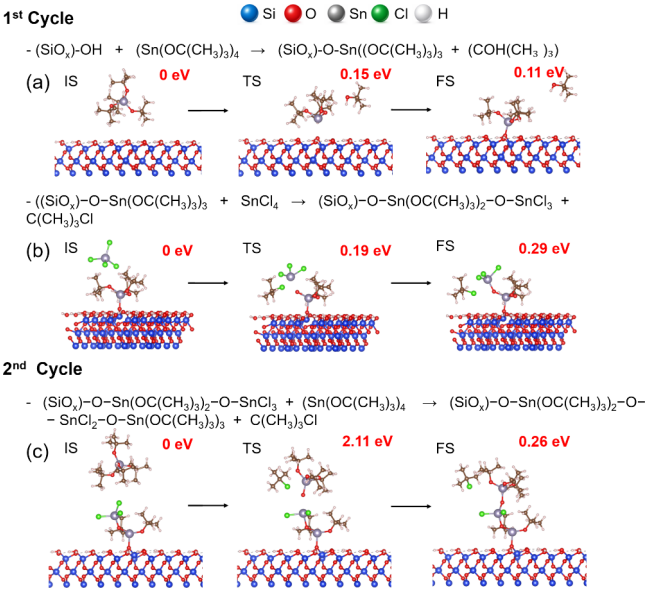

Figure 5. Proposed ligand-exchange pathways for the ALD growth of Sn species on hydroxylated SiO_2, showing the optimized geometries of the initial (IS), transition-like (TS), and final (FS) configurations for each elementary step. (a) First half-cycle: adsorption of the Sn alkoxide precursor on a surface –OH group, followed by proton-transfer-assisted ligand exchange and formation of an interfacial Sn–O bond. (b) Reaction of the chlorinated Sn precursor with the surface-bound species, leading to additional Sn–O bond formation and surface functionalization. (c) Subsequent coordination step illustrating further growth of the Sn-containing layer through ligand exchange and structural rearrangement at the interface. Adsorption, Sn–O bond formation, and ligand elimination through a proton-transfer mechanism.

(IS), $SnCl_4$ approaches the surface with one chloride ligand oriented toward the Sn–O bond of the surface-bound *tert*-butoxide group. The precursor retains its tetrahedral coordination geometry, and the interaction at this stage is weak. At the transition state (TS), O–C bond cleavage of the surface-bound *tert*-butoxide begins, a Sn–Cl bond elongates, and a bridging Sn–O–Sn interaction forms, reflecting concerted bond reorganization (TS energy 0.19 eV). In the final state (FS), a *tert*-butoxide ligand detaches and reacts with chloride to form 2-chloro-2-methylpropane (C_4H_9Cl), while a bridging Sn–O–Sn–Cl surface motif is established (FS energy 0.29 eV).

Next, during the second ALD cycle $Sn(OtBu)_4$ reacts with the Cl-terminated surface via ligand exchange (Figure 5c), removing

https://doi.org/10.1021/acsami.6c07074
ACS Appl. Mater. Interfaces XXXX, XXX, XXX–XXX

chloride through O–C bond cleavage to form 2-chloro-2-methylpropane (C_4H_9Cl) while simultaneously forming new O–Sn–O bonds that extend the Sn–O network. This pathway, characterized by the continuous evolution of the volatile byproduct C_4H_9Cl, was experimentally confirmed by ^{1}H NMR analysis of different $Sn(OtBu)_4/SnCl_4$ mixtures, which showed the corresponding C_4H_9Cl signal at 1.62 ppm for both a 1:1 precursor ratio and in the presence of excess $SnCl_4$ (Figure S11), supporting the proposed sequential ligand-exchange mechanism. However, it should be noted that these solution-phase experiments do not directly represent the surface chemistry occurring under actual ALD conditions. The main purpose of these experiments is to provide supporting evidence that the proposed reaction pathway is chemically reasonable.

Energetically, the large size of the resulting adsorbate complex generates significant steric hindrance, reflected in the much higher TS energy of 2.11 eV compared to panels (a) and (b). After structural relaxation, the FS reaches 0.26 eV, corresponding to a locally stable configuration in which C_4H_9Cl is accommodated more effectively away from the surface-active adsorption sites. The high TS energy arises because the reaction was modeled assuming a single substitution event without removing other surface-fragment molecules, resulting in a highly congested configuration. Under realistic conditions, multiple ligand-exchange reactions across the surface fragments would reduce the overall energy. Therefore, the calculated TS energy of 2.11 eV should be regarded as an upper-bound estimate rather than a physical activation barrier for the ALD process.

Similarly, the positive final-state (FS) energies obtained do not necessarily indicate that the proposed half-reactions are thermodynamically unfavorable under ALD conditions. As noted above, the simulations were limited to the ligand-exchange step on a saturated surface model, where the reaction by-product (C_4H_9Cl) remains near the surface and cannot fully diffuse away. Consequently, the calculated FS energies reflect the relaxed configuration immediately after ligand exchange and before the purge step, rather than the fully equilibrated state of the complete ALD cycle. In the experimental process, volatile by-products are removed during purging, further stabilizing the system. However, they were not explicitly included in the present calculations, which were designed to identify the elementary ligand-exchange mechanism governing film growth. The FS energies should be interpreted as describing the energetics of the elementary ligand-exchange event rather than the overall thermodynamics of the ALD cycle.

The simplified stepwise reactions describing the interactions between the precursors, $SnCl_4$ and $Sn(OtBu)_4$ can be generalized as follows:

For $SnCl_x$:

$$\text{Si–O–Sn–O}t\text{Bu} + \text{SnCl}_x \rightarrow \text{Si–O–Sn–O–Sn–Cl} + t\ \text{BuCL} \quad (1)$$

For $Sn(OtBu)_x$:

$$\text{Si–O–Sn–O–Sn–Cl} + \text{Sn}(O t\text{Bu})_x \rightarrow \text{Si–O–Sn–O–Sn–O–Sn–O–}t\text{Bu} + t\text{BuCl} \quad (2)$$

Here, the evolution of the volatile byproduct (tBuCl or C_4H_9Cl) demonstrates that ligand exchange between Sn–Cl and Sn–OtBu groups drives the formation of Sn–O–Sn–O bonds. This provides direct evidence for the feasibility of SnO_2 network growth from these precursors without requiring an external oxidizing agent.

It should be noted, however, that only a single ligand-exchange event was considered in each reaction step to reduce computational cost. The double-exchange pathway is also possible, although likely sterically hindered, and could in principle occur in parallel with the single-exchange mechanism. Steric hindrance from bulky *tert*-butoxide ligands (molecular size ≈ 9 Å) limits chloride removal at certain surface sites, where the distance between Cl atoms in the surface-bound $SnCl_3$ fragment is approximately 3.55 Å. This leads to residual chloride, as well as carbon and hydrogen impurities from partially unreacted ligands. This also explains the low Sn/O ratio (~1.6, below the stoichiometric value of 2) observed in the as-grown films, as ligand-exchange reactions do not proceed to completion. This mechanism is consistent with experimental observations and highlights the need for post-deposition thermal treatment to promote additional Sn–O bond formation between residual Sn–Cl and Sn–OtBu groups trapped within the structure, and subsequent removal of Cl, C, and H impurities.

Our analysis provides atomistic insight into the growth pathway of SnO_2 under oxidant-free ALD conditions and rationalizes the stepwise evolution of the Sn–O framework observed during film formation, complementing and supporting the experimental evidence presented in the previous sections.

2.4. Computational Investigation of the Influence of Annealing Atmosphere on SnO_2

To elucidate the role of the annealing atmosphere in the evolution of residual chlorine and oxygen-related defects, Non-Covalent Interaction (NCI) analysis was performed between the Cl-terminated rutile SnO_2 surface and O_2, N_2, and Ar molecules (Figure 6).

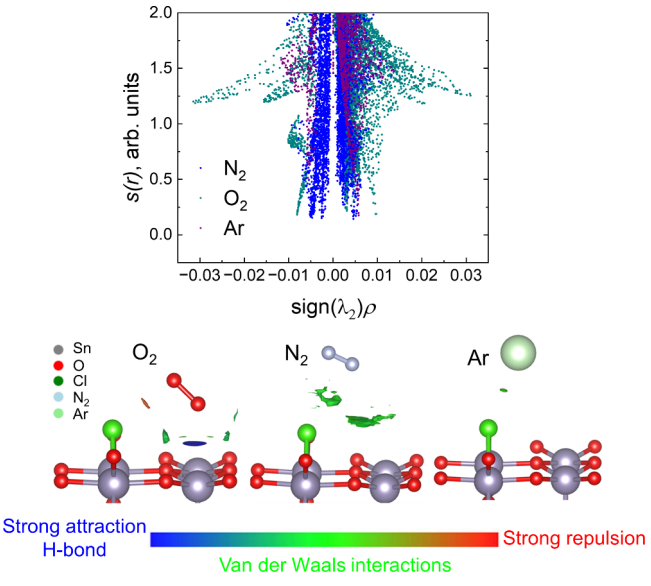

Figure 6. Non-Covalent Interaction (NCI) analysis of gas molecules interacting with the Cl-contaminated rutile SnO_2 surface during post-deposition annealing. Top panels: reduced density gradient (RDG) vs sign(λ_2)ρ scatter plots for O_2, N_2, and Ar atmospheres. Bottom panels: corresponding real-space NCI isosurfaces.

https://doi.org/10.1021/acsami.6c07074
ACS Appl. Mater. Interfaces XXXX, XXX, XXX–XXX

The non-covalent interaction (NCI) analysis is a useful tool for differentiating and visualizing the interactions present in the studied systems.[43] The analysis is based on the reduced density gradient (RDG), which is defined as.

$$s(r) = \frac{1}{2(3\pi^2)^{\frac{1}{3}}} \frac{|\nabla\rho(r)|}{\rho(r)^{\frac{4}{3}}} \quad (3)$$

where $\rho(r)$ is the electron density and $\nabla\rho(r)$ is the electron density gradient.

Within this framework, the nature of the interaction is characterized by the second eigenvalue (λ_2) of the Hessian matrix of the electron density. The sign of λ_2 distinguishes attractive and repulsive interactions: $\lambda_2 < 0$ corresponds to attractive interactions (e.g., hydrogen bonding or covalent character), whereas $\lambda_2 > 0$ is associated with nonbonding or sterically repulsive interactions. Values of $\text{sign}(\lambda_2)\rho(r)$ close to zero are characteristic of weak van der Waals (vdW) interactions. By plotting $s(r)$ as a function of $\text{sign}(\lambda_2)\rho(r)$, non-covalent interactions can be identified in regions of low reduced density gradient and low electron density. Moreover, the strength of the interaction increases with increasing electron density, allowing differentiation between weak dispersive contacts and stronger attractive interactions.

The RDG vs $\text{sign}(\lambda_2)\rho$ plots reveal clear differences in interaction strength and character. For O_2, the distribution extends into the negative $\text{sign}(\lambda_2)\rho$ region, indicating the presence of attractive interactions with partial directionality. In contrast, N_2 exhibits weaker features near to $\text{sign}(\lambda_2)\rho \approx 0$, consistent with weaker stabilization. Ar shows a distribution almost entirely centered around $\text{sign}(\lambda_2)\rho \approx 0$, characteristic of purely dispersive van der Waals interactions without directional bonding character.

The NCI isosurfaces support this interpretation. The color scale distinguishes interaction types: blue regions correspond to strong attractive interactions, green to weak van der Waals stabilization, and red to repulsive regions. For O_2, localized green-to-light-blue regions appear between the molecule and undercoordinated surface Sn atoms, evidencing a higher propensity for surface coordination. N_2 predominantly displays diffuse green isosurfaces, reflecting weaker, less directional interactions. In the case of Ar, the isosurfaces are sparse and uniformly green, confirming its non-reactive, dispersive nature.

These interaction differences provide a framework for interpreting the experimental trends in oxygen vacancy concentration, which follow the order: Air (21–22%) < O_2 (24–26%) < Ar (25–29%). Under Ar, the gas acts primarily as a sweep gas, facilitating the thermal removal of volatile chlorine species via mass transport, but does not supply a chemically active species to stabilize the surface afterward. Consequently, although chlorine is effectively displaced, the absence of reactive oxygen may limit compensation of oxygen-related defects, leading to the highest observed vacancy concentration.

In oxygen-containing atmospheres, the situation differs. O_2 exhibits stronger, more localized surface interactions, indicating a greater tendency to engage in surface coordination than Ar. However, the lowest vacancy concentration is not obtained under pure O_2 but under air, which consists predominantly of N_2 and O_2. This suggests that the most efficient defect minimization arises from a combined effect: N_2 contributes to gas-flow dynamics and transport (similar to a carrier or sweep component), while O_2 provides the reactive species that interact with exposed surface sites. The synergy between mass transport and reactive coordination may promote more effective chlorine displacement while simultaneously enabling better stabilization of the surface lattice, resulting in the lowest oxygen vacancy concentration observed for air-treated films.

The ERDA results further support this interpretation. Although O_2 provides a reactive environment for surface stabilization, the O_2-annealed films exhibit higher residual H (6.1 at%), C (2.7 at%), and Cl contents than the Ar- and air-annealed samples. While the present results do not allow the origin of these species to be unequivocally identified, their simultaneous presence suggests incomplete removal of ligand-derived residues rather than the incorporation of new contaminants during annealing. This interpretation is consistent with the NCI analysis, which indicates stronger O_2-surface interactions than for Ar or N_2. Such interactions may promote surface stabilization but simultaneously reduce the efficiency of desorption of volatile residual species. Consequently, the lower conductivity observed for the O_2-annealed films, despite their comparable oxygen-vacancy concentration, may be associated with the higher concentration of residual H-, C-, and Cl-containing species, which can act as charge-trapping or electron-scattering centers. In contrast, the air atmosphere combines the sweeping effect of N_2 with the chemical activity of O_2, facilitating both the removal of volatile chlorine-containing species and the stabilization of the oxide network. This combined effect provides a plausible explanation for the lower impurity content and improved electrical performance observed after air annealing.

2.5. Electrical Properties of SnO_2 Films

Distinct differences in electrical behavior are observed as a function of the annealing atmosphere, arising from variations in grain size and oxygen vacancy concentration induced under different thermal environments. Figure 7a shows the electrical DC conductivity (σ_{DC}) as a function of temperature. At low

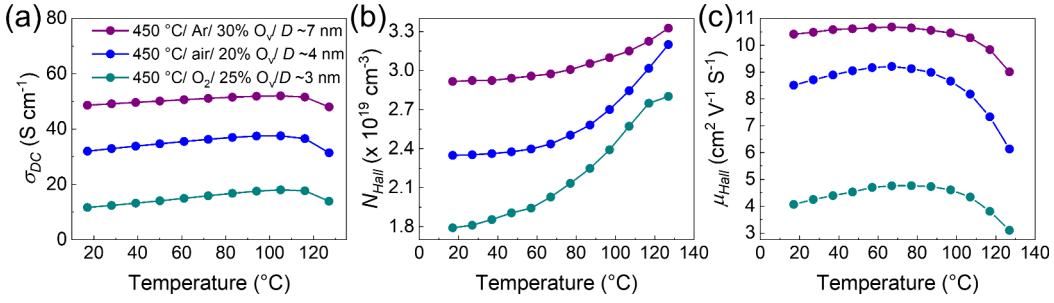

Figure 7. Four probe resistivity and hall measurements of SnO_2 films annealed in Ar (purple), in air (blue) and O_2 (green) measured in the range from 17–125 °C: (a) electrical conductivity (σ_{DC}), (b) carrier concentration (N_{Hall}), and (c) electron mobility (μ_{Hall}).

https://doi.org/10.1021/acsami.6c07074
ACS Appl. Mater. Interfaces XXXX, XXX, XXX–XXX

temperatures, the films exhibit semiconducting behavior, with σ_{DC} increasing moderately with T. Above ~100 °C, however, σ_{DC} begins to decrease, reflecting metal-like transport characteristics. This crossover does not indicate a true semiconductor-to-metal phase transition but rather a change in the dominant charge-transport mechanism, likely driven by reduced mobility due to enhanced phonon scattering and oxygen-related surface effects at elevated temperatures.[26]

The absolute magnitude of σ_{DC} is strongly influenced by the annealing atmosphere. Films annealed in Ar, with the largest grain sizes (>10 nm) and an average crystallite size (D) of ~7 nm, exhibit the highest conductivity (~50 S cm^{-1}). Films annealed in air, with grain sizes below 10 nm and crystallite sizes of ~4 nm, display moderate conductivities (~30 S cm^{-1}). In contrast, O_2-annealed films, with the smallest crystallites (~3 nm) and higher levels of hydrogen and carbon impurities, show the lowest conductivity (~12 S cm^{-1}).

Hall measurements confirm the n-type nature of the films, with carrier concentration increasing exponentially with temperature (Figure 7b). This behavior is characteristic of thermally activated donor states, primarily oxygen vacancies and related defect levels. At lower temperatures, partial ionization limits the number of free electrons in the conduction band, whereas at elevated temperatures, additional donor states are ionized, releasing electrons. Grain-boundary potential barriers also influence this behavior; at low-temperatures carrier trapping reduces the effective carrier density, whereas at higher temperatures, carriers gain sufficient thermal energy to overcome these barriers. Consequently, the observed temperature dependence reflects both thermally activated donor ionization and progressive release of carriers from grain-boundary traps.

The carrier concentration, N_{Hall}, is moderately influenced by the oxygen-vacancy content. Ar-annealed films (25–29% O_V) exhibit the highest carrier density (2.9×10^{19} cm^{-3} at room temperature) followed by air-annealed films (21–22% O_V, $N_{hall} = 2.35 \times 10^{19}$ cm^{-3}). Despite comparable vacancy levels (24–26% O_V), O_2-annealed films present a lower carrier density (1.81×10^{19} cm^{-3}), likely due to higher levels of hydrogen and carbon impurities, as identified by ERDA, which introduce carrier-trapping or charge-compensation effects.

Carrier mobility (μ_{Hall}, in Figure 7c) mirrors the trend in σ_{DC}. At low temperatures, thermal activation and reduced grain-boundary trapping enhance mobility, whereas above ~100 °C, phonon scattering and thermally induced disorder dominate, leading to mobility reduction. The highest mobility is observed in Ar-annealed films (10.5 cm^2 V^{-1} s^{-1}), followed by air-annealed (8.7 cm^2 V^{-1} s^{-1}) and O_2-annealed (4.3 cm^2 V^{-1} s^{-1}). Notably, while carrier density varies by less than a factor of two, mobility varies by more than a factor of two, indicating that conductivity is primarily governed by scattering and microstructural connectivity (grain sizes) rather than carrier generation alone. These findings are further supported by Drude modeling of the infrared region of the ellipsometry spectra, in which the free-carrier footprint can also be analyzed from an optical perspective, additional discussion can be found in Section S.4 of the Supporting Information.

The electrical performance of Ar-, air-, and O_2-annealed SnO_2 films is consistent with values reported for other SnO_2 ALD processes (see Table S2) and with those obtained via alternative fabrication methods.[11,44] For the as-grown films, determination of conductivity is challenging because the films are highly resistive due to their amorphous nature, exhibiting conductivity values in the range of 10^{-3}–10^{-4} S cm^{-1}. Similar conductivity values (~10^{-4} S cm^{-1}) have been reported for SnO_2 films deposited by low-temperature ALD processes (≤100 °C).[28,29,31] Detailed comparison of the optical, morphological, compositional, and electrical properties of our SnO_2 films with those reported in the literature can be found in Table S2 of the Supporting Information.

2.6. Optical Characterization of SnO_2 Films

Optical properties were assessed using spectroscopic ellipsometry, which measures changes in the polarization of light upon reflection. Fitting the experimental spectra to an appropriate optical model representing the sample structure (see Experimental Section) yielded the complex refractive index ($n + ik$) and film thickness (see Table 3). The number of ALD cycles was adjusted to produce films with thicknesses that closely matched the expected nominal values. A reduction in thickness was observed after annealing, accompanied by an increase in the density of the films (Figure S1b). Similar behavior has been previously reported in the literature[19] with increasing deposition temperature. In our case, the post-annealing treatment leads not only to crystallization but also to an increase in density and a reduction in thickness, as impurities are eliminated and new Sn–O bonds are formed.

The calculated transmission spectra (Figure 8a) reveal high transparency (85–90%) across the visible-to-near-infrared region (500–2500 nm) for as grown and annealed films. Ar-annealed films exhibit slightly reduced transparency near the absorption edge. This behavior is commonly associated with oxygen vacancies, which introduce donor states below the conduction band and enable absorption of lower-energy photons.[45,46] The oxygen-vacancy concentration in these films is approximately 30%. The as-grown amorphous films also display a similar behavior, albeit less pronounced, despite having even higher oxygen-vacancy levels (~45–47%). This observation suggests the presence of an additional contribution in the Ar-annealed films, which we attribute to phonon scattering at

Table 3. Summary of Thickness (t), Crystallite Size (D), Surface Roughness (S_{qz}), Oxygen-Vacancy Content, and Direct and Indirect Optical Band Gaps Determined from Spectroscopic Ellipsometry Measurements[a]

sample	t (nm)	S_q (nm)	D (nm)	O_V %	E_g directon (eV)	E_g indirecton (eV)	σ_{DC} (S cm^{-1})	N_{Hall} (cm^{-3})	μ_{Hall} (cm^2 V^{-1} s^{-1})
as-grown	57.2	0.35		47		3.86	10^{-3}–10^{-4}		
450°C/Ar	56.1	1.82	~7	30	4.00	3.29	50	$2.92 \cdot 10^{19}$	10.5
450°C/O_2	52.4	0.43	~3	25	3.97	3.18	10	$1.81 \cdot 10^{19}$	4.25
450°C/air	42.3	1.76	~4	20	4.04	3.50	30	$2.35 \cdot 10^{19}$	8.71

[a]Together with hall-effect transport properties, including electrical conductivity (σ_{DC}), (N_{Hall}), and carrier mobility (μ_{Hall}), for the SnO_2 films investigated in this work.

https://doi.org/10.1021/acsami.6c07074
ACS Appl. Mater. Interfaces XXXX, XXX, XXX–XXX

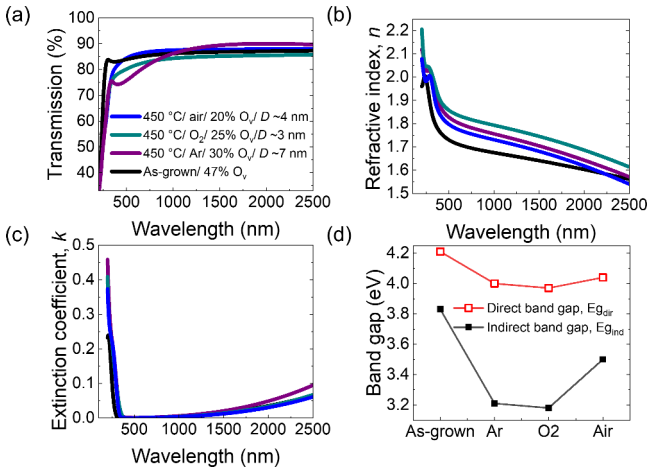

Figure 8. (a) Absorption coefficient, (b) refraction index, n and (c) extinction coefficient, k of SnO_2 films as-grown (black), and annealed SnO_2 films at 450 °C under Ar (purple), O_2 atmosphere (green), and in ambient conditions (blue). (d) Optical band gaps obtained from Tauc plots, considering both indirect and direct transitions.

well-defined grain boundaries formed after crystallization, consistent with their larger grain sizes (>10 nm and $D \sim 7$ nm).[10]

The refractive index, n, and extinction coefficient, k, shown in Figure 8b,c, provide further insight into the optical properties of the films. Both the as-grown and annealed films exhibit maximum refractive indices ($n \sim 2.0$–2.2) in the UV region (200–400 nm), consistent with values reported for SnO_2 in the literature.[4,47] As the wavelength increases, n decreases rapidly and then more gradually beyond 500 nm, characteristic of normal dispersion behavior.

At a wavelength of 550 nm, the as-grown SnO_2 film exhibits a refractive index of $n = 1.70$. This relatively low refractive index is consistent with the reduced effective density of the as-grown film, arising from its amorphous structure, lower packing efficiency, and higher impurity content, as evidenced by the XRD/XRR, XPS, and ERDA analyses. Similar low refractive indices have been reported for SnO_2 films deposited at temperatures below 200 °C, where incomplete precursor reactions result in lower film density and higher residual impurity concentrations.[19,24,28,47] Following annealing, the refractive index at 550 nm increases to $n = 1.80$–1.85, reflecting enhanced structural ordering, film densification, and impurity removal induced by the thermal treatment.

The extinction coefficient, k, which quantifies optical absorption losses, exhibits a sharp decrease in the UV region (200–400 nm), reflecting the transition from strong absorption near the fundamental absorption edge of SnO_2 ($E_g \sim 3.6$ eV) to a weakly absorbing regime at longer wavelengths. In the visible range (400–700 nm), k remains near zero, consistent with the high optical transparency required for optoelectronic applications. In the infrared region (>1200 nm), k gradually increases due to free-carrier absorption, as described by the Drude model.[48] This increase is most pronounced for the Ar-annealed film, which exhibits the highest carrier concentration, N_{Hall}, according to Hall-effect measurements (Figure 7b), but is observed in all films, including the as-prepared amorphous samples. The origin of this infrared absorption is discussed further in relation to the dominant charge-transport mechanisms in SnO_2 films in Section S.4 of the Supporting Information.

The optical band gaps, (E_g), including both indirect and direct transitions, were extracted from Tauc analysis (Figure S8a–h). The resulting indirect, E_g^{ind}, and direct band gap, E_g^{dir}, values of the as-grown and annealed films are plotted in Figure 8d. The indirect band gaps range from 3.18 to 3.86 eV, whereas direct E_g values range from 3.97 to 4.21 eV. Theoretically, SnO_2 is predicted to exhibit an allowed direct band gap in the range of 3.68–4.07 eV, depending on the orientation of the polarized light relative to the tetragonal crystallographic axis. In addition, lower-energy indirect electronic transitions have also been predicted.[49]

For the crystalline (annealed) samples, the fundamental band gap is direct and remains essentially invariant with respect to the annealing atmosphere, with a value of approximately 4.0 eV, see Figure S8b–d. The small difference between the Ar- and O_2-annealed samples (~30 meV) is likely due to the Burstein-Moss effect,[50] as supported by electrical measurements. This shift can be described by $\Delta E_{BM} = (\hbar^2/2m^*)(3\pi^2 N)^{2/3}$, assuming an electron effective mass for SnO_2 of ~0.3 m_0. Using carrier concentrations of 2.9×10^{19} cm^{-3} for the Ar-annealed sample and 1.8×10^{19} cm^{-3} for the O_2-annealed sample, the calculated shift is consistent with the experimentally observed difference in band gap.

The indirect band gap values, shown in Figure S8f–h, do not represent a true fundamental gap but rather defect-assisted sub-bandgap absorption, varying from 3.2 eV for O_2, 3.3 eV for Ar, and 3.5 eV for air. This trend reflects differences in the density of optically active defect states (e.g., oxygen-vacancy-related states contributing to sub-gap absorption).[28–30,45,46] In particular, the O_2-treated sample exhibits the strongest contribution of such states, leading to the largest apparent reduction in the indirect gap despite its lower electrical conductivity, indicating optically active but electrically inactive defects.

In contrast, for the as-grown film, crystal momentum conservation is relaxed due to the absence of long-range order, rendering the direct/indirect distinction nonrigorous. The $(\alpha h\nu)^2$ plot does not exhibit a well-defined linear region near the absorption edge, which is masked by defect-related absorption and appears shifted toward higher photon energies (~4.21 eV, see Figure S8a). Therefore, no direct band gap is assigned in the present work, although similarly high direct band gap values (>4.0 eV) are commonly reported and assigned to amorphous SnO_2 films deposited by other low-temperature ALD processes (see Table S2); only Mullings et al.[32] reports an indirect band gap. According to the above reasoning, the lowest-energy absorption onset is taken as the fundamental gap (~3.9 eV, in Figure S8e), which is slightly lower than that of the annealed samples. This difference (~0.1 eV) lies within the uncertainty of the extrapolation method and should not be interpreted as evidence of a significant band-gap shift. Rather, it is likely attributable to the limitations of the fitting procedure and the broadness of the absorption edge.

2.7. Proof-of-Concept Applications of Water-/Oxidant-Free ALD SnO_2 Process

To demonstrate the potential of our water- and oxidant-free ALD SnO_2 process, we explored applications in scenarios where conventional ALD approaches may be limited, such as sensitivity to moisture, reactive oxidants, high deposition temperatures,

https://doi.org/10.1021/acsami.6c07074
ACS Appl. Mater. Interfaces XXXX, XXX, XXX–XXX

or incompatibility with hydrophobic substrates. These proof-of-concept tests highlight the versatility and stability of the hereby developed SnO_2 ALD process in practical device architectures.

One particularly promising application is the integration of amorphous SnO_2 within multilayer stacks, where it can serve as a protective buffer layer during the fabrication of electrodes[28] and solar cells.[29] In addition, thin amorphous SnO_2 interlayers may act as energy-filtering barriers for low-energy charge carriers while simultaneously enhancing phonon scattering and reducing the overall thermal conductivity of the structure. This concept is analogous to the approach reported by Yang et al.[21]

Within this context, we evaluated the compatibility of the water- and oxidant-free SnO_2 ALD process with $SnSe_2$, a material that we have previously deposited by ALD at similarly low temperatures.[51] In addition to their compatible thermal budgets, both processes employ $SnCl_4$ as the tin precursor, which, although not essential, simplifies the implementation of multilayer growth. More importantly, the absence of an actual oxidizing agent during the SnO_2 deposition minimizes the risk of selenium oxidation and the formation of Se–O species at the interface, thereby preserving the integrity of the $SnSe_2$ layer.

This was confirmed through TEM and XPS analyses of a $SnO_2/SnSe_2/SnO_2$ sandwich structure consisting of approximately 7 nm SnO_2/21 nm $SnSe_2$/7 nm SnO_2. The high-resolution scanning TEM image of the multilayer shown in Figure 9a clearly displays a remarkably uniform interface between the $SnSe_2$ and SnO_2 layers. Moreover, the $SnSe_2$ layer maintains its well-ordered crystalline structure, with the c-axis oriented normal to the substrate as evidenced by the [001] lattice planes in horizontal direction, consistent with our previous reports.[51] No observable changes in crystal orientation or indications of defect formation are detected following either the SnO_2 deposition process or the subsequent post-deposition annealing treatment at 250 °C.

The XRD diffractogram of the same sandwich structure (Figure S12a) further confirms the preservation of the crystalline quality over a much larger sampled area. The diffraction pattern exhibits a strong and highly oriented (001) reflection at 16.87° 2θ, characteristic of c-axis-oriented $SnSe_2$. In addition, well-defined diffraction fringes are observed around the main Bragg peak, indicating excellent crystalline coherence, low interface roughness, and high structural quality of the $SnSe_2$ layer. These results demonstrate that the SnO_2 deposition and subsequent thermal treatment do not compromise the structural integrity of the $SnSe_2$ film.

As emphasized throughout this work, a key objective was to prevent oxidation of the two-dimensional semiconductor at the interface. Preliminary XPS analysis of the $SnO_2/SnSe_2/SnO_2$ multilayer did not reveal detectable Se–O species (Figure 9b), based on the Sn 3d, O 1s, and Se 3d spectra. In particular, no additional Se 3d components were observed in the higher binding-energy region (~58–60 eV), where oxidized selenium species are typically expected. These results suggest that the interface remained chemically stable throughout both deposition and thermal processing. The corresponding C 1s and Cl 2p spectra are provided in Figure S12b.

Additional support for this conclusion is provided by Hall effect measurements, see Figure S12c, which show no significant degradation of the electrical transport properties of the $SnSe_2$ layer after incorporation into the multilayer stack. The absence of interfacial oxidation is expected to be particularly beneficial for preserving carrier mobility and minimizing interface-related scattering. Although the present study is based on a simplified multilayer architecture, the results demonstrate the feasibility of combining oxidant-free SnO_2 with $SnSe_2$ in heterostructure based devices. Future work will explore this material combination in greater detail by systematically varying the relative $SnSe_2$ and SnO_2 layer thicknesses and by

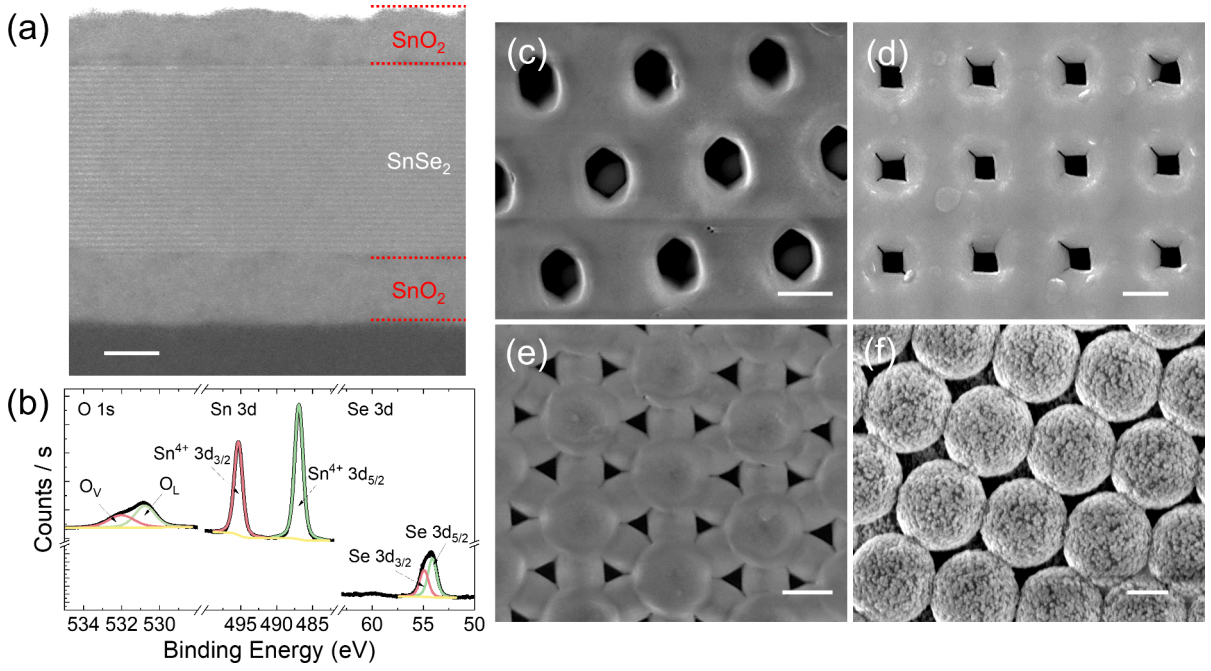

Figure 9. (a) Cross-sectional high-resolution scanning transmission electron microscopy image of $SnO_2/SnSe_2/SnO_2$ sandwich stack. Scale bar 10 nm. (b) XPS analysis of Sn 3d, Se 3d, and O 1s in the multilayer stack. (c–e) AAO membranes with different pore morphologies: circular (c), square (d), and triangular (e), coated with 250 cycles of SnO_2. (f) Polymer opal spheres coated with 300 cycles of SnO_2. Scale bar 200 nm (c–f).

https://doi.org/10.1021/acsami.6c07074
ACS Appl. Mater. Interfaces XXXX, XXX, XXX–XXX

investigating ultrathin SnO_2 interlayers in the 1–5 nm range, which may provide additional opportunities for interface engineering and transport-property optimization.

Another aspect investigated was the conformality of the SnO_2 coating on nonplanar substrates. To evaluate this, a series of substrates with different geometries were examined. In particular, 250 cycles of SnO_2 were deposited onto porous alumina substrates featuring distinct pore morphologies (Figure 9c–e). The resulting coatings were used to assess the ability of the process to achieve uniform coverage on complex three-dimensional architectures. SEM images of the uncoated anodic aluminum oxide (AAO) membranes are provided in Figure S13a–c. Corresponding SEM images of the annealed SnO_2/AAO samples are also included, Figure S13d–f, demonstrating that the coating remains highly conformal after thermal treatment at 450 °C and providing further evidence of the robustness of the deposition process on complex porous structures.

Finally, we tested our low-temperature, water/oxidant-free recipe on polymeric opal substrates, as shown in Figure S14a (uncoated). These self-assembled opals consist of polystyrene particles, which according to the manufacturer's specifications, are thermally stable below 100 °C and exhibit hydrophobic surface properties. Their hydrophobic surface may pose challenges for the implementation of water-based deposition processes, while exposure to strong oxidizing agents (e.g., H_2O_2 or O_2 plasma) could potentially induce degradation of the polymer template. As such, they represent a demanding yet relevant platform for assessing the conformality and effectiveness of this water- and oxidant-free SnO_2 deposition process on polymer-based nanostructured substrates. Figure 9g shows successful coating of the spheres after 300 ALD cycles of SnO_2. Cross-sectional SEM images (Figure S14c–e), taken from the top to the bottom of the structure up to the top surface, reveal complete infiltration and conformal coverage throughout the opal film, which has a total thickness of approximately 25 μm (Figure S14b). More important, no degradation of the polymeric substrate is observed after deposition. In future work, the SnO_2 films could be crystallized via a post-annealing step that simultaneously removes the polymeric template, thereby combining template removal and film crystallization into a single processing step.

Collectively, these results demonstrate the versatility of the developed ALD SnO_2 process across different material systems and substrate architectures. These experiments serve as proof-of-concept demonstrations of the potential utility of mild initial processing conditions, combining water-/oxidant-free chemistry with low deposition temperatures, for selected material systems, which can be followed by postdeposition annealing to tailor the structural and functional properties of the deposited films.

3. CONCLUSIONS

Herein, we report a novel ALD route for the growth of SnO_2 thin films under mild, oxidant-free deposition conditions, where no external oxidizing agents (e.g., H_2O, H_2O_2, O_3 or O_2 plasma) are employed. This approach is particularly beneficial for deposition on sensitive substrates, such as carbon-based and polymeric materials, and in multilayer architectures, where preventing oxidation of the underlying materials is crucial. The process operates at temperatures below 100 °C, providing a relatively low thermal budget that allows initial deposition of SnO_2 also on temperature-sensitive substrates.

As is typical for SnO_2 films deposited at low temperatures (≤200 °C), the as-deposited films are predominantly amorphous and contain appreciable amounts of H, C, and Cl impurities. Post-deposition treatments at 450 °C under Ar, O_2, and air atmospheres are highly effective in enhancing the crystallinity, reducing impurities, and enhancing the films' electronic properties. Drude modeling reveals that the most significant effect of annealing conditions is the generation of percolative pathways that facilitate DC conduction in the films. These pathways are strongly correlated with the crystallinity and grain size of the films, which can be controlled by varying the annealing atmospheres. Consequently, it is possible to selectively enhance the carrier mobility, carrier density, and conductivity of SnO_2 thin films.

The treated films exhibit mobilities in the range of 4–11 $cm^2 V^{-1} s^{-1}$, conductivities of 12–50 S cm^{-1}, and carrier concentrations on the order of 10^{19} cm^{-3}. Combined with wide band gaps (~4. 0 eV), low optical losses, and high transparency in the UV-Vis range, these films on their own hold significant promise for advanced optoelectronic applications, including transparent electron transport layers and photonic technologies.

Beyond this, the compatibility of the reported process with stack architectures, organic-based substrates, and complex geometries was evaluated. The preliminary results provide an initial indication of the suitability of our process to overcome some of the limitations of conventional SnO_2 deposition routes when applied to non-conventional or sensible substrates, by enabling initial film deposition under conditions that minimize thermal and oxidative exposure. While subsequent postdeposition annealing can be employed when required to achieve the desired functional properties.

In addition to the experimental findings, the reaction pathways during ALD growth were further corroborated by density functional theory (DFT) calculations. These computational studies provide critical insights into the underlying mechanisms of the oxidant-free growth process, linking precursor chemistry to film quality and defect formation. On the one hand, they confirm the formation of an extended –Sn–O–Sn–O– network via ligand-exchange reactions between Sn–Cl and Sn–O*t*Bu species. On the other hand, they reveal limitations in ligand-exchange reactions due to steric hindrance from the bulky $Sn(OtBu)_4$ precursor.

Additional computational investigations of the annealing conditions provide strong evidence that different atmospheres play distinct roles: argon (Ar) primarily facilitates impurity removal through mass transport, whereas O_2 and air can also chemically interact with the films, enhancing impurity removal and improving film quality.

This combined experimental-theoretical approach establishes a robust framework for optimizing SnO_2 deposition on sensitive substrates and offers valuable guidance for future developments in the field of transparent, high-performance materials.

4. METHODS

4.1. Material Synthesis

4.1.1. SnO_2 on Si and SiO_2 Substrates. SnO_2 thin films were deposited using a thermal ALD system (Veeco Savannah S100) onto both bare p-type Si substrates and Si substrates coated with a 100 nm thermally grown SiO_2 layer. Two precursors were used: tin (IV) chloride ($SnCl_4$, purchased from Strem) and tin(IV) *tert*-butoxide ($Sn(OtBu)_4$, from Sigma Aldrich-Merck), maintained at room

https://doi.org/10.1021/acsami.6c07074
ACS Appl. Mater. Interfaces XXXX, XXX, XXX–XXX

temperature and 60 °C, respectively. Ultra-high purity nitrogen served as the carrier gas at a constant flow rate of 10 sccm. The deposition temperature was varied between 70 and 120 °C.

Before deposition, substrates were cleaned via sequential ultrasonication in acetone, isopropanol, ethanol, and deionized water for 5 min each. This was followed by a 10-minute treatment in a UV-ozone cleaner (Ossila, Sheffield, UK). To investigate ALD growth characteristics, the pulse duration of each precursor was systematically varied. $SnCl_4$ pulses of 0.005, 0.01, 0.05, and 0.1 s were tested while keeping $Sn(OtBu)_4$ fixed at 0.15 s. Subsequently, $Sn(OtBu)_4$ pulse durations of 0.05, 0.10, 0.15, and 0.20 s were evaluated with $SnCl_4$ held constant at 0.01 s. The optimized ALD cycle consisted of a 0.15 s pulse of $Sn(OtBu)_4$ followed by a 10 s N_2 purge, then a 0.01 s $SnCl_4$ pulse followed by another 10 s N_2 purge. A total of 800 cycles were performed per deposition.

As-deposited SnO_2 films were amorphous. Post-deposition annealing was conducted at 450 °C in a two-zone tubular furnace in a quartz tube (OTF-1200X, MTI Corporation) under different atmospheres: argon (Ar), oxygen (O_2), and ambient air (with the tube ends left open for air annealing). Before heating, the furnace was evacuated to a base pressure of 10^{-3}–10^{-2} mbar. Samples were placed at the center of the furnace in alumina (Al_2O_3) crucibles. The heating rate was 5 °C min^{-1} until the target temperature was reached, which was then maintained for 5 h. Samples were allowed to cool naturally to below 50 °C. For Ar and O_2 annealing, the gases were continuously flowed at a pressure of 3 mbar. Air annealing was conducted at ambient pressure with open tube ends.

4.1.2. Multilayer Sandwich Structure. $SnO_2/SnSe_2/SnO_2$ stacks were fabricated using 100 ALD cycles of SnO_2 under the optimized conditions described above, followed by 200 ALD cycles of $SnSe_2$ (deposition conditions described elsewhere[51]), and capped with an additional 100 ALD cycles of SnO_2. After deposition, the samples were annealed at 250 °C for 30 min on a hot plate.

4.1.3. SnO_2 on Non-Planar Substrates. AAO membranes with circular, square and triangular pore shapes were obtained from our partners at HZDR[52,53] and subsequently coated with 250 ALD cycles of SnO_2. Self-assembled opaline substrates were fabricated as reported elsewhere[18,54] and then, coated with 300 ALD cycles of SnO_2.

4.2. Characterization and Measurements

The morphology of the as-deposited and annealed films was evaluated by field-emission scanning electron microscopy (FESEM; Sigma300-ZEISS). The composition of the SnO_2 films was studied by X-ray photoemission spectroscopy (XPS) and time-of-flight elastic recoil detection analysis (ToF-ERDA). XPS measurements were carried out in an ultrahigh vacuum chamber (ESCALAB 250Xi by Thermo Scientific, base pressure: 2×10^{-10} mbar) using an XR6-monochromated Al Kα source ($h\nu$ = 1486.6 eV) and a pass energy of 20 eV. A spot size of 650 μm was utilized for the analysis. Before analysis, surface cleaning was performed using Ar^+ ion etching (4000 eV, mode: cluster) for 300 s. Spectral fitting and background correction were performed using the Avantage Data System software (Thermo Fisher Scientific). Peak calibration was referenced to the C–C bond at 284.8 eV. ToF-ERD was performed using a 13.6 MeV $^{63}Cu^{7+}$ beam. Recoiled atoms, emitted from different film depths, were detected via a time-of-flight-energy (ToF-E) telescope, enabling mass identification and energy calculation from time-of-flight. The angle between the sample normal and the incoming beam was 70°, while the scattering angle was 40.6°. The analyzed area was approximately 3×3 mm^2. The data were analyzed with Potku 2.3.1,[55] which iteratively refines the composition profile based on beam parameters, stopping powers, and measurement geometry. The resulting concentration depth profiles are convoluted by system resolution and physical effects such as energy loss straggling, multiple scattering and surface roughness.

In situ XRD measurements were performed on the as-deposited SnO_2 films using a Rigaku SmartLab SE diffractometer with Cu Kα radiation. Measurements were carried out over different temperature intervals with the temperature continuously increasing from 30 to 500 °C at a heating rate of 5 °C min^{-1}. Diffraction patterns were collected over a 2θ range of 5° to 70°, using a step size of 0.02° (2θ) and a scan speed of 10.00° min^{-1}. Ex situ XRD measurements of films annealed at 450 °C and 800 °C were conducted over a 2θ range of 5°–50° with a step size of 0.02° (2θ) to investigate the crystallinity and phase composition of the SnO_2 films. X-ray reflectometry (XRR) measurements were performed using a Philips X'Pert MRD PRO system (Netherlands) equipped with a Cu Kα radiation source, Eulerian cradle, and a fixed divergence slit (1/32°).

High-angle annular dark-field scanning transmission electron microscopy (HAADF-STEM) was carried out using a Talos F200X G2 (S) TEM instrument (ThermoFisher Scientific) operating at 200 kV. For the HAADF-STEM images, a probe semi-convergence angle of 10.5 mrad was employed and a camera length was set to cover an angular range with the HAADF detector between 40 mrad and 200 mrad.

AFM images were obtained with a Dimension ICON microscope from Bruker working in the Peak Force Tapping mode and using a Scanasyst-Air probe also from Bruker (nominal frequency 70 kHz, spring constant 0.4 N/m, and tip radius 5 nm). AFM scan size was 500 nm × 500 nm in all cases. Raw AFM images were processed using the open-source software Gwyddion to correct for tilt and scan-line artifacts. RMS roughness values (S_q) were obtained after performing these corrections.

The optical properties of both as-grown SnO_2 thin films and annealed at 450 °C deposited on p-type crystalline silicon were investigated using spectroscopic ellipsometry (SE). UV-Vis-NIR SE measurements were performed to obtain the ellipsometric angles Ψ and Δ, as well as the depolarization spectra, over the wavelength range of 200–2500 nm (corresponding to photon energies of 6.2–0.39 eV) with a step size of 10 nm.

The measurements were carried out using a VASE vertical variable-angle-of-incidence rotating-analyzer ellipsometer (J.A. Woollam), equipped with a computer-controlled Berek wave-plate retarder (Automatic Retarder). Data were collected at three angles of incidence: 55°, 65°, and 75°. Monochromatic light was generated by an HS-190 double monochromator fitted with three sets of gratings covering the near-infrared (NIR), visible (VIS), and quartz-ultraviolet (QUV) spectral regions. A 75 W Xe short-arc lamp (Hamamatsu L10873) was used as the light source, producing a ∼1 mm beam spot at normal incidence.

Infrared Spectroscopy Ellipsometry (IRSE) was used to study the photon energy range 4000–1000 cm^{-1} (2500–10,000 nm) with a step size of 8 cm^{-1}, with incident angles of 55°, 65°, and 75°. IRSE measurements were carried out on a J.A. Woollam IR-VASE Mark II ellipsometer, which integrates a Fourier Transform Infrared (FTIR) interferometer source with a rotating compensator ellipsometer. During the measurement, the compensator was rotated 360° in a series of steps and an intensity spectrum related with the sample optical properties was recorded at each step. The Ψ and Δ spectra for each sample were then determined from a combination of the intensity spectra from each position of the compensator.

For electrical characterization, samples were deposited on Si substrates with 100 nm SiO_2. Electrical transport measurements were carried out between 300 and 2 K in a DynaCool cryostat using the Electrical Transport Option (ETO) in a Van der Pauw geometry, together with an automated switchbox (ASB102, all from Quantum Design). Electrical contacts were made manually using freshly cleaned indium wire (Ø = 0.15 mm, 99%, HMW Hauner GmbH & Co. KG), attached by applying gentle pressure.

^1H NMR spectra were measured with 500 MHz Avance II spectrometer (Bruker) in CDCl3 (99.9%; Deutero) at 298 K. ^1H chemical shifts are reported as values in ppm referenced to residual solvent ($CHCl_3$, δ = 7.24 ppm).

5. COMPUTATIONAL METHODS

5.1. DFT Molecular Simulations

To investigate the two key surface-precursor interactions governing the atomic layer deposition growth of SnO_2, a SiO_2 surface was used as a representative substrate in combination with the Sn-based precursors

https://doi.org/10.1021/acsami.6c07074
ACS Appl. Mater. Interfaces XXXX, XXX, XXX–XXX

(tin(IV) chloride ($SnCl_4$) and tin(IV) *tert*-butoxide [$Sn(OtBu)_4$]). This framework allows a direct atomistic evaluation of the elementary reaction steps that define the ALD cycle.

All calculations were performed using first-principles density functional theory (DFT) within the Projector Augmented Wave (PAW) formalism, as implemented in the Vienna Ab initio Simulation Package (VASP).[56−59] The exchange-correlation interactions were treated using the generalized gradient approximation (GGA) with the Perdew-Burke-Ernzerhof (PBE) functional.[60] A plane-wave cutoff energy of 500 eV was employed. Self-consistent field (SCF) calculations were converged to an energy tolerance of 10^{-6} eV, and all atomic structures were fully relaxed until the residual forces on each atom were below 0.01 eV $Å^{-1}$.

Brillouin zone integrations were carried out using a 3 × 3 × 1 Monkhorst-Pack *k*-point mesh.[61] To eliminate spurious interactions between periodically repeated slabs, a vacuum region of 15 Å was introduced along the direction perpendicular to the surface plane.[62,63] The reaction mechanisms associated with the ALD process were further investigated using a proposed ligand-exchange pathway for the two elementary reaction steps.[64] Grimme's DFT-D3 dispersion correction was included in all calculations (IVDW = 11 in VASP) to account for long-range Van der Waals interactions.[65] Additionally, NCI (non-covalent interaction) analysis was employed to analyze the role of the annealing atmosphere in the removal of residual chloride species.[43]

5.2. SE and IRSE Data Modeling

Modeling of experimental SE and IRSE data was performed making use of the WVASE software package (J.A. Woollam Co., Inc.). For the determination of the optical constants and thickness of the SnO_2 films, an optical model consisting of a SnO_2 thin film deposited on a crystalline silicon substrate was employed. A 2 nm thick native silicon oxide layer was included in the model between the film and the substrate. The optical constants of both the silicon substrate and the native oxide layer were taken from the built-in libraries of the software.

The dielectric function of the SnO_2 thin film was modeled using a Drude term accounting for free-carrier intraband absorption in the NIR, a Tauc-Lorentz oscillator describing the fundamental interband transition, and Gaussian oscillators representing higher-energy interband transitions. A high-energy Gaussian oscillator was included to ensure Kramers-Kronig consistency beyond the measured spectral range.

The transmittance spectra of ALD SnO_2 thin films were simulated to confirm their optical transparency within the visible and near-infrared spectral ranges. In simulations, the non-transparent silicon substrate in the visible range was replaced by a quartz substrate with high transparency in the visible and near-infrared regions. The simulations were developed using WVASE software based on an optical model consisting of a thin film of SnO_2 and a quartz substrate. The optical constants of the quartz substrate were obtained from the ellipsometry and optical transmission experiments of the clean substrate. On the other hand, the optical constants and thicknesses of the different SnO_2 thin films were obtained from the spectroscopic ellipsometry experiments, as previously described, carried out on Si substrates.

■ ASSOCIATED CONTENT

Supporting Information

The Supporting Information is available free of charge at https://pubs.acs.org/doi/10.1021/acsami.6c07074.

Additional experimental data, including in situ XRD measurements, XRR, XPS, AFM analyses, SEM, and ^1H NMR spectra; complementary computational models used in the DFT simulations; and the complete Drude formalism equations for interpreting electrical conductivity (DOCX)

■ AUTHOR INFORMATION

Corresponding Authors

Alejandra Ruiz-Clavijo – *Leibniz Institute for Solid State and Materials Research Dresden, Dresden 01069, Germany;* orcid.org/0000-0002-9585-6658; Email: a.ruiz.de.clavijo.garcia.serrano@ifw-dresden.de

Kornelius Nielsch – *Leibniz Institute for Solid State and Materials Research Dresden, Dresden 01069, Germany; Institute of Applied Physics, Technische Universität Dresden, Dresden 01062, Germany;* orcid.org/0000-0003-2271-7726; Email: k.nielsch@ifw-dresden.de

Authors

Amin Bahrami – *Leibniz Institute for Solid State and Materials Research Dresden, Dresden 01069, Germany;* orcid.org/0000-0001-8851-7351

Jonathan E. Rodriguez Hueso – *Centro de Nanociencias y Nanotecnología, Universidad Nacional Autónoma de México, Km.107, Apdo. Postal 14. Carretera Tijuana-Ensenada, Ensenada, Baja California 22860, Mexico;* orcid.org/0009-0003-1903-258X

Jaakko Julin – *Department of Physics, University of Jyväskylä, Jyväskylä 40014, Finland;* orcid.org/0000-0003-4376-891X

Noel Israel – *Leibniz Institute for Solid State and Materials Research Dresden, Dresden 01069, Germany*

Angelika Wrzesińska-Lashkova – *Leibniz Institute for Solid State and Materials Research Dresden, Dresden 01069, Germany; Chair for Emerging Electronic Technologies, Technische Universität Dresden, Dresden 01187, Germany*

Daniel Wolf – *Leibniz Institute for Solid State and Materials Research Dresden, Dresden 01069, Germany; Leibniz Institute for Polymer Research Dresden, Dresden 01069, Germany;* orcid.org/0000-0001-5000-8578

Nithin Thonakkara James – *Institute for Applied Materials, Karlsruhe Institute of Technology (KIT), Kaiserstraße 12, Karlsruhe 76131, Germany*

Sebastian Lehmann – *Leibniz Institute for Solid State and Materials Research Dresden, Dresden 01069, Germany;* orcid.org/0000-0001-7913-9387

Jonathan Guerrero-Sánchez – *Centro de Nanociencias y Nanotecnología, Universidad Nacional Autónoma de México, Km.107, Apdo. Postal 14. Carretera Tijuana-Ensenada, Ensenada, Baja California 22860, Mexico;* orcid.org/0000-0003-1457-9677

R. Ponce-Perez – *Centro de Nanociencias y Nanotecnología, Universidad Nacional Autónoma de México, Km.107, Apdo. Postal 14. Carretera Tijuana-Ensenada, Ensenada, Baja California 22860, Mexico;* orcid.org/0000-0002-6726-1569

Alexey A. A. Popov – *Leibniz Institute for Solid State and Materials Research Dresden, Dresden 01069, Germany;* orcid.org/0000-0002-7596-0378

Manuel Dominguez – *Department of Condensed Matter Physics, University of Cadiz, Puerto Real, Cadiz E11510, Spain; IMEYMAT: Institute of Research on Electron Microscopy and Materials, University of Cadiz, Puerto Real, Cadiz E11510, Spain;* orcid.org/0000-0002-7889-7220

Yana Vaynzof – *Leibniz Institute for Solid State and Materials Research Dresden, Dresden 01069, Germany; Chair for Emerging Electronic Technologies, Technische Universität*

Dresden, Dresden 01187, Germany; orcid.org/0000-0002-0783-0707

Kaline P. Furlan – *Institute for Applied Materials, Karlsruhe Institute of Technology (KIT), Kaiserstraße 12, Karlsruhe 76131, Germany;* orcid.org/0000-0003-4032-2795

Eduardo Blanco – *Department of Condensed Matter Physics, University of Cadiz, Puerto Real, Cadiz E11510, Spain; IMEYMAT: Institute of Research on Electron Microscopy and Materials, University of Cadiz, Puerto Real, Cadiz E11510, Spain;* orcid.org/0000-0002-2234-1477

Complete contact information is available at: https://pubs.acs.org/doi/10.1021/acsami.6c07074

Author Contributions

The manuscript was written through contributions of all authors. All authors have given approval to the final version of the manuscript.

Funding

This work was supported by the Program of Collaborative Research Centers in Germany (grant no. SFB 1415). The computational part of this work was partially supported by the DGAPA-UNAM (grant numbers IG101124 and IA100226) and by the DGTIC-UNAM (grant numbers LANCAD-UNAM-DGTIC-422 and LANCAD-UNAM-DGTIC-368). Funding by the German Research Foundation (Deutsche Forschungsgemeinschaft, DFG) via the "Responsible Electronics in the Climate Change Era – REC^2" Cluster of Excellence (EXC 3035, Project-ID 533607596) is gratefully acknowledged.

Notes

The authors declare no competing financial interest.

■ ACKNOWLEDGMENTS

The authors thank Almut Pöhl for FIB sample preparation and Katja Berger for assistance with SEM imaging of charging samples (opals). The authors also thank Dr. Rui Xu from Helmholtz-Zentrum Dresden-Rossendorf (HZDR) for providing the AAO templates.

■ REFERENCES

(1) Marichy, C., Silva, R. M.; Pinna, N.; Willinger, M.; Donato, N.; Neri, G. (Invited) Non-Aqueous Atomic Layer Deposition of SnO_2 for Gas Sensing Application. *ECS Trans.* **2018**, *86*(6), 55.

(2) Nguyen, V. H.; Akbari, M.; Sekkat, A.; Ta, H. T.; Resende, J.; Jiménez, C.; Musselman, K. P.; Muñoz-Rojas, D. Atmospheric atomic layer deposition of SnO_2 thin films with tin(ii) acetylacetonate and water. *Dalton Trans.* **2022**, *51* (24), 9278–9290.

(3) Kumar, K. D. A.; Valanarasu, S.; Jeyadheepan, K.; Kim, H. S.; Vikraman, D. Evaluation of the physical, optical, and electrical properties of SnO_2: F thin films prepared by nebulized spray pyrolysis for optoelectronics. *J. Mater. Sci.: Mater. Electron.* **2018**, *29* (5), 3648–3656.

(4) Manifacier, J. C.; De Murcia, M.; Fillard, J. P.; Vicario, E. Optical and electrical properties of SnO_2 thin films in relation to their stoichiometric deviation and their crystalline structure. *Thin Solid Films* **1977**, *41* (2), 127–135.

(5) Hu, L.; Yan, J.; Liao, M.; Wu, L.; Fang, X. Ultrahigh External Quantum Efficiency from Thin SnO_2 Nanowire Ultraviolet Photodetectors. *Small* **2011**, *7* (8), 1012–1017.

(6) Chen, Q.-Z.; Zhang, Z. X.; Fu, W. Q.; Duan, J. R.; Yang, Y. X.; Chen, C. N.; Lien, S. Y. Low Resistivity and High Carrier Concentration in SnO_2 Thin Films: The Impact of Nitrogen–Hydrogen Annealing Treatments. *Nanomaterials* **2025**, *15* (13), 986.

(7) Mun, H.; Yang, H.; Park, J.; Ju, C.; Char, K. High electron mobility in epitaxial SnO_{2-x} in semiconducting regime. *APL Mater.* **2015**, *3* (7), 076107.

(8) Yang, G.; Chen, C.; Yao, F.; Chen, Z.; Zhang, Q.; Zheng, X.; Ma, J.; Lei, H.; Qin, P.; Xiong, L.; Ke, W.; Li, G.; Yan, Y.; Fang, G. Effective Carrier-Concentration Tuning of SnO_2 Quantum Dot Electron-Selective Layers for High-Performance Planar Perovskite Solar Cells. *Adv. Mater.* **2018**, *30* (14), 1706023.

(9) Shao, M.; Liu, J.; Ding, W.; Wang, J.; Dong, F.; Zhang, J. Oxygen vacancy engineering of self-doped SnO_{2-x} nanocrystals for ultrasensitive NO_2 detection. *J. Mater. Chem. C* **2020**, *8* (2), 487–494.

(10) Lee, J.-H.; You, Y. J.; Saeed, M. A.; Kim, S. H.; Choi, S. H.; Kim, S.; Lee, S. Y.; Park, J. S.; Shim, J. W. Undoped tin dioxide transparent electrodes for efficient and cost-effective indoor organic photovoltaics (SnO_2 electrode for indoor organic photovoltaics). *NPG Asia Mater.* **2021**, *13* (1), 43.

(11) Li, X.; Tan, F.; Zhang, C.; Zhou, J.; Guo, Z.; Yang, Y.; Xie, Y.; Cao, X.; Feng, Y.; Li, L. Research Progress on Transparent Conductive Properties of SnO_2 Thin Films. *Coatings* **2026**, *16* (1), 23.

(12) Hossain, M. A.; Khoo, K. T.; Cui, X.; Poduval, G. K.; Zhang, T.; Li, X.; Li, W. M.; Hoex, B. Atomic layer deposition enabling higher efficiency solar cells: A review. *Nano Mater. Sci.* **2020**, *2* (3), 204–226.

(13) Marichy, C.; Donato, N.; Willinger, M. G.; Latino, M.; Karpinsky, D.; Yu, S. H.; Neri, G.; Pinna, N. Tin Dioxide Sensing Layer Grown on Tubular Nanostructures by a Non-Aqueous Atomic Layer Deposition Process. *Adv. Funct. Mater.* **2011**, *21* (4), 658–666.

(14) Nishijima, Y.; Ueno, K.; Juodkazis, S.; Mizeikis, V.; Misawa, H.; Tanimura, T.; Maeda, K. Inverse silica opal photonic crystals for optical sensing applications. *Opt. Express* **2007**, *15* (20), 12979–12988.

(15) Guddala, S.; Shadak Alee, K.; Narayana Rao, D. Fabrication of multifunctional SnO_2 and SiO_2-SnO_2 inverse opal structures with prominent photonic band gap properties. *Opt. Mater. Express* **2013**, *3*(3), 407–417.

(16) Gun, Y.; Song, G. Y.; Quy, V. H. V.; Heo, J.; Lee, H.; Ahn, K. S.; Kang, S. H. Joint Effects of Photoactive TiO_2 and Fluoride-Doping on SnO_2 Inverse Opal Nanoarchitecture for Solar Water Splitting. *ACS Appl. Mater. Interfaces* **2015**, *7* (36), 20292–20303.

(17) Maho, A.; Lobet, M.; Daem, N.; Piron, P.; Spronck, G.; Loicq, J.; Cloots, R.; Colson, P.; Henrist, C.; Dewalque, J. Photonic Structuration of Hybrid Inverse-Opal TiO_2—Perovskite Layers for Enhanced Light Absorption in Solar Cells. *ACS Appl. Energy Mater.* **2021**, *4* (2), 1108–1119.

(18) Hedrich, C.; James, N. T.; Maragno, L. G.; Lima, V., de; González, S. Y. G.; Blick, R. H.; Zierold, R.; Furlan, K. P. Enhanced Photocatalytic Properties and Photoinduced Crystallization of TiO_2–Fe_2O_3 Inverse Opals Fabricated by Atomic Layer Deposition. *ACS Appl. Mater. Interfaces* **2024**, *16* (36), 46964–46974.

(19) Heo, J.; Kim, S. B.; Gordon, R. G. Atomic layer deposition of tin oxide with nitric oxide as an oxidant gas. *J. Mater. Chem.* **2012**, *22* (11), 4599–4602.

(20) Drozd, V. E.; Aleskovski, V. B. Synthesis of conducting oxides by ML-ALE. *Appl. Surf. Sci.* **1994**, *82*, 591–594.

(21) Yang, J.; Mukherjee, S.; Lehmann, S.; Krahl, F.; Wang, X.; Potapov, P.; Lubk, A.; Ritschel, T.; Geck, J.; Nielsch, K. Low-Temperature ALD of SbO_x/Sb_2Te_3 Multilayers with Boosted Thermoelectric Performance. *Small* **2024**, *20* (10), 2306350.

(22) Lee, G. R.; Seong, M.; Kim, S.; Pyeon, K.; Chung, R. B. Conductive SnO_{2-x} thin films deposited by thermal ALD with H_2O reactant. *Vacuum* **2022**, *200*, 111018.

(23) Xu, L.; He, L.; Yang, L.; Zhang, Z.; Guo, S.; Yang, Z.; Wang, P.; Geng, F.; Gao, G.; Sun, C.; Ralchenko, V.; Zhu, J. Plasma treatment to tailor growth and photoelectric performance of plasma-enhanced atomic layer deposition SnOx infrared transparent conductive thin films. *Surf. Coat. Technol.* **2020**, *403*, 126414.

(24) Elam, J.W.; Baker, D. A.; Hryn, A. J.; Martinson, A. B.; Pellin, M. J.; Hupp, J. T. Atomic layer deposition of tin oxide films using tetrakis(dimethylamino) tin. *J. Vac. Sci. Technol., A* **2008**, *26*(2), 244–252.
(25) Nanayakkara, C. E.; Liu, G.; Vega, A.; Dezelah, C. L.; Kanjolia, R. K.; Chabal, Y. J. Reaction Mechanisms of the Atomic Layer Deposition of Tin Oxide Thin Films Using Tributyltin Ethoxide and Ozone. *Langmuir* **2017**, *33* (24), 5998–6004.
(26) Tran Thi My, H.; Nguyen, N. L.; Mac, T. K.; Duong, D. A.; Nguyen, T. T.; Duong, A. T.; Bui, H. V.; Nguyen, V. H. Impact of air exposure on growth rate and electrical properties of SnO_2 thin films by atmospheric pressure spatial atomic layer deposition. *J. Phys. D: Appl. Phys.* **2024**, *57* (2), 025303.
(27) Du, X.; Du, Y.; George, S. M. In situ examination of tin oxide atomic layer deposition using quartz crystal microbalance and Fourier transform infrared techniques. *J. Vac. Sci. Technol., A* **2005**, *23*(4), 581–588.
(28) Behrendt, A.; Friedenberger, C.; Gahlmann, T.; Trost, S.; Becker, T.; Zilberberg, K.; Polywka, A.; Görrn, P.; Riedl, T. Highly robust transparent and conductive gas diffusion barriers based on tin oxide. *Adv. Mater.* **2015**, *27* (39), 5961–5967.
(29) Hoffmann, L.; Brinkmann, K. O.; Malerczyk, J.; Rogalla, D.; Becker, T.; Theirich, D.; Shutsko, I.; Gorrn, P.; Riedl, T. Spatial atmospheric pressure atomic layer deposition of tin oxide as an impermeable electron extraction layer for perovskite solar cells with enhanced thermal stability. *ACS Appl. Mater. Interfaces* **2018**, *10* (6), 6006–6013.
(30) Choi, D. W.; Maeng, W. J.; Park, J. S. The conducting tin oxide thin films deposited via atomic layer deposition using Tetrakis-dimethylamino tin and peroxide for transparent flexible electronics. *Appl. Surf. Sci.* **2014**, *313*, 585–590.
(31) Hoffmann, L.; Theirich, D.; Schlamm, D.; Hasselmann, T.; Pack, S.; Brinkmann, K. O.; Rogalia, D.; Peters, S.; Räupke, A.; Gargouri, H.; Riedl, T. Atmospheric pressure plasma enhanced spatial atomic layer deposition of SnO_x as conductive gas diffusion barrier. *J. Vac. Sci. Technol., A* **2018**, *36* (1), 01A112.
(32) Mullings, M. N.; Hägglund, C.; Bent, S. F. Tin oxide atomic layer deposition from tetrakis (dimethylamino) tin and water. *J. Vac. Sci. Technol., A* **2013**, *31* (6), 061503.
(33) Chung, W.-Y.; Lee, D.-D.; Sohn, B.-K. Effects of added TiO_2 on the characteristics of SnO_2-based thick film gas sensors. *Thin Solid Films* **1992**, *221* (1), 304–310.
(34) Wang, W.; Niu, J.; Ao, L. Large-scale synthesis of single-crystal rutile SnO_2 nanowires by oxidizing SnO nanoparticles in flux. *J. Cryst. Growth* **2008**, *310* (2), 351–355.
(35) Padova, P., De; Fanfoni, M.; Larciprete, R.; Mangiantini, M.; Priori, S.; Perfetti, P. A synchrotron radiation photoemission study of the oxidation of tin. *Surf. Sci.* **1994**, *313* (3), 379–391.
(36) Du, W.; Wan, Z.; Zhu, J.; Liu, X.; Chen, L.; Li, S.; Kang, N.; Wang, C. In situ one step growth of amorphous tin oxide electron transport layer for high-performance perovskite solar cells. *RSC Adv.* **2024**, *14* (18), 12650–12657.
(37) Zhang, J.; Wei, X.; Zhao, J.; Zhang, Y.; Wang, L.; Huang, J.; She, H.; Wang, Q.; Wang, Q. Electronegative Cl– modified BiVO4 photoanode synergized with nickel hydroxide cocatalyst for high-performance photoelectrochemical water splitting. *Chem. Eng. J.* **2023**, *454*, 140081.
(38) Hao, L.; Kang, L.; Huang, H.; Ye, L.; Han, K.; Yang, S.; Yu, H.; Batmunkh, M.; Zhang, Y.; Ma, T. Surface-Halogenation-Induced Atomic-Site Activation and Local Charge Separation for Superb CO_2 Photoreduction. *Adv. Mater.* **2019**, *31* (25), 1900546.
(39) Gong, W.; Guo, H.; Zhang, H.; Yang, J.; Chen, H.; Wang, L.; Hao, F.; Niu, X. Chlorine-doped SnO_2 hydrophobic surfaces for large grain perovskite solar cells. *J. Mater. Chem. C* **2020**, *8* (33), 11638–11646.
(40) Lu, Z.; Wang, Y.; Zhang, J.; Du, X.; Sun, W. Defect passivation of SnO_2 doped with 2-FN for high-performance perovskite detectors. *J. Mater. Chem. C* **2025**, *13* (8), 3969–3977.
(41) Guo, H.; Xiang, W.; Fang, Y.; Li, J.; Lin, Y. Molecular Bridge on Buried Interface for Efficient and Stable Perovskite Solar Cells. *Angew. Chem., Int. Ed.* **2023**, *62* (34), e202304568.
(42) Liang, J.; Chen, Z.; Yang, G.; Wang, H.; Ye, F.; Tao, C.; Fang, G. Achieving High Open-Circuit Voltage on Planar Perovskite Solar Cells via Chlorine-Doped Tin Oxide Electron Transport Layers. *ACS Appl. Mater. Interfaces* **2019**, *11* (26), 23152–23159.
(43) Rodríguez-Hueso, J. E.; Borbón-Nuñez, H. A.; Ponce-Pérez, R.; Hoat, D. M.; Takeuchi, N.; Tiznado, H.; Guerrero-Sánchez, J. Atomic-scale study of TiO_2-GR nanohybrid formation by ALD: the effect of the gas phase precursor. *Nanoscale Adv.* **2023**, *5* (20), 5476–5486.
(44) Deva Arun Kumar, K.; Valanarasu, S.; Capelle, A.; Nar, S.; Karim, W.; Stolz, A.; Aspe, B.; Semmar, N. Nanostructured Oxide (SnO_2, FTO) Thin Films for Energy Harvesting: A Significant Increase in Thermoelectric Power at Low Temperature. *Micromachines* **2024**, *15* (2), 188.
(45) Wang, J.; Wang, Z.; Huang, B.; Ma, Y.; Liu, Y.; Qin, X.; Zhang, X.; Dai, Y. Oxygen Vacancy Induced Band-Gap Narrowing and Enhanced Visible Light Photocatalytic Activity of ZnO. *ACS Appl. Mater. Interfaces* **2012**, *4* (8), 4024–4030.
(46) Yang, Y.; Wang, Y.; Yin, S. Oxygen vacancies confined in SnO_2 nanoparticles for desirable electronic structure and enhanced visible light photocatalytic activity. *Appl. Surf. Sci.* **2017**, *420*, 399–406.
(47) Farva, U.; Kim, J. Growth temperature-dependent morphological, optical, and electrical study of SnO_2 thin film by atomic layer deposition. *Mater. Chem. Phys.* **2021**, *267*, 124584.
(48) Dressel, M.; Grüner, G. *Electrodynamics of Solids: Optical Properties of Electrons in Matter*; Cambridge University Press, **2002**.
(49) Arlinghaus, F. J. Energy bands in stannic oxide (SnO_2). *J. Phys. Chem. Solids* **1974**, *35* (8), 931–935.
(50) Zhai, C.-H.; Zhang, R. J.; Chen, X.; Zheng, Y. X.; Wang, S. Y.; Liu, J.; Dai, N.; Chen, L. Y. Effects of Al doping on the properties of ZnO thin films deposited by atomic layer deposition. *Nanoscale Res. Lett.* **2016**, *11* (1), 407.
(51) Ruiz-Clavijo, A.; Bahrami, A.; Charvot, J.; Lehmann, S.; Julin, J.; Wolf, D.; Giebeler, L.; Wrzesińska-Lashkova, A.; Pieck, F.; Outon, J.; Tonner-Zech, R.; Bureš, F.; Vaynzof, Y.; Blanco, E.; Nielsch, K. Thickness-Driven Modulation of Electronic Transport in $SnSe_2$-grown Films by Low-Temperature Atomic Layer Deposition. *Adv. Electron. Mater.* **2026**, *12* (2), e00560.
(52) Xu, R.; Zeng, Z.; Lei, Y. Well-defined nanostructuring with designable anodic aluminum oxide template. *Nat. Commun.* **2022**, *13* (1), 2435.
(53) Xu, R.; Zhao, H.; Jin, H.; Wang, Z.; Zhang, Z.; Xu, S.; Zeng, Z.; Wang, S.; Lei, Y. Scalable fabrication of geometry-tunable self-aligned superlattice photonic crystals for spectrum-programmable light trapping. *Nano Energy* **2019**, *58*, 543–551.
(54) Gehensel, R. J.; Zierold, R.; Schaan, G.; Shang, G.; Petrov, A. Y.; Eich, M.; Blick, R.; Krekeler, T.; Janssen, R.; Furlan, K. P. Improved thermal stability of zirconia macroporous structures via homogeneous aluminum oxide doping and nanostructuring using atomic layer deposition. *J. Eur. Ceram. Soc.* **2021**, *41* (7), 4302–4312.
(55) Arstila, K.; Julin, J.; Laitinen, M. I.; Aalto, J.; Konu, T.; Kärkkäinen, S.; Rahkonen, S.; Raunio, M.; Itkonen, J.; Santanen, J.-P.; Tuovinen, T.; Sajavaara, T. Potku–New analysis software for heavy ion elastic recoil detection analysis. *Nucl. Instrum. Methods Phys. Res., Sect. B* **2014**, *331*, 34–41.
(56) Kresse, G.; Furthmüller, J. Efficient iterative schemes for ab initio total-energy calculations using a plane-wave basis set. *Phys. Rev. B* **1996**, *54* (16), 11169–11186.
(57) Kresse, G.; Furthmüller, J. Efficiency of ab-initio total energy calculations for metals and semiconductors using a plane-wave basis set. *Comput. Mater. Sci.* **1996**, *6* (1), 15–50.
(58) Blöchl, P. E. Projector augmented-wave method. *Phys. Rev. B* **1994**, *50* (24), 17953–17979.

(59) Kresse, G.; Joubert, D. From ultrasoft pseudopotentials to the projector augmented-wave method. *Phys. Rev. B* **1999**, *59* (3), 1758–1775.
(60) Perdew, J. P.; Burke, K.; Ernzerhof, M. Generalized Gradient Approximation Made Simple. *Phys. Rev. Lett.* **1996**, *77* (18), 3865–3868.
(61) Monkhorst, H. J.; Pack, J. D. Special points for Brillouin-zone integrations. *Phys. Rev. B* **1976**, *13* (12), 5188–5192.
(62) Wu, D.; Min, T.; Zhou, J.; Li, C.; Ma, G.; Lu, G.; Xia, M.; Gu, Z. Effect of Substrate symmetry on the dendrite morphology of MoS_2 Film synthesized by CVD. *Sci. Rep.* **2017**, *7* (1), 15166.
(63) Loaiza-Orduz, Á.; Araujo-López, E.; Urresta, J. D.; Llano-Restrepo, M. DFT computational study of the tetragonal (P4/nmm) WO3 (001) Surface. *Ing. Compet.*, **2018**, *20*, 83–94.
(64) Henkelman, G.; Uberuaga, B.P.; Jónsson, H.A climbing image nudged elastic band method for finding saddle points and minimum energy paths. *J. Chem. Phys.* **2000**, *113*(22), 9901–9904.
(65) Grimme, S.; Antony, J.; Ehrlich, S.; Krieg, S. A consistent and accurate ab initio parametrization of density functional dispersion correction (DFT-D) for the 94 elements H–Pu. *J. Chem. Phys.* **2010**, *132* (15), 154104.

https://doi.org/10.1021/acsami.6c07074
ACS Appl. Mater. Interfaces XXXX, XXX, XXX–XXX